1   **Affinity hierarchies and amphiphilic proteins underlie the**
2   **co-assembly of nucleolar and heterochromatin condensates**

3   **Authors**

4   Srivarsha Rajshekar[1], Omar Adame-Arana[2,3], Gaurav Bajpai[2,4], Serafin Colmenares[1],
5   Kyle Lin[1], Samuel Safran[2], Gary H Karpen[1,5]
6   [1] Department of Molecular and Cell Biology, University of California Berkeley, Berkeley,
7   USA
8   [2] Department of Chemical and Biological Physics, Weizmann Institute of Science,
9   Rehovot, Israel
10   [3] Max Planck Institute for the Physics of Complex Systems, Dresden, Germany
11   [4] Department of Physics, Northeastern University, Boston, USA
12   [5] Division of Biological Sciences and the Environment, Lawrence Berkeley National
13   Laboratory, Berkeley, USA

14   **Correspondence: gkarpen@berkeley.edu**

15   **Abstract**

16   Nucleoli are surrounded by Pericentromeric Heterochromatin (PCH), reflecting a close
17   spatial association between the two largest biomolecular condensates in eukaryotic
18   nuclei. Nucleoli are the sites of ribosome synthesis, while the repeat-rich PCH is essential
19   for chromosome segregation, genome stability, and transcriptional silencing. How and
20   why these two distinct condensates co-assemble is unclear. Here, using high-resolution
21   live imaging of *Drosophila* embryogenesis, we find that *de novo* establishment of PCH
22   around the nucleolus is highly dynamic, transitioning from the nuclear edge to surrounding
23   the nucleolus. Eliminating the nucleolus by removing the ribosomal RNA genes (rDNA)
24   resulted in increased PCH compaction and subsequent reorganization into a toroidal
25   structure. In addition, in embryos lacking rDNA, some nucleolar proteins were
26   redistributed into new bodies or 'neocondensates', including enrichment in the PCH
27   toroidal hole. Combining these observations with physical modeling revealed that
28   nucleolar-PCH associations can be mediated by a hierarchy of interaction strengths
29   between PCH, nucleoli, and 'amphiphilic' protein(s) that have affinities for both nucleolar
30   and PCH components. We validated this model by identifying a candidate amphiphile, a
31   DEAD-Box RNA Helicase called Pitchoune, whose depletion or mutation of its PCH
32   interaction motif disrupted PCH-nucleolar associations. Together, this study unveils a
33   dynamic program for establishing nucleolar-PCH associations during animal
34   development, demonstrates that nucleoli are required for normal PCH organization, and
35   identifies Pitchoune as an amphiphilic molecular link required for PCH-nucleolar
36   associations.

Introduction

The eukaryotic nucleus is organized into different membrane-less compartments or biomolecular condensates that assemble via phase separation or similar mechanisms driven by multivalent interactions between their constituent molecules [1,2]. An individual condensate concentrates several macromolecules, including structured and intrinsically disordered proteins and nucleic acids [3,4]. Condensates with the same components can nucleate and grow at different cellular locations and coarsen by fusions into larger clusters, whereas those with distinct compositions do not mix [5]. Nevertheless, in the crowded environment of the nucleus, different condensates display close, conserved associations to form higher-order complex structures [6]. Although many studies have examined the formation and function of individual condensates, how distinct interacting condensates form and impact each other *in vivo* is less clear. This study addresses this question in the context of the two largest nuclear condensates, the nucleolus and heterochromatin.

The nucleolus is the site of ribosome synthesis with additional functions in cell cycle progression, stress response, and protein sequestration [7]. The nucleolus assembles on chromosomal loci with transcribing ribosomal RNA genes (rDNA) and recruits specific factors involved in ribosomal RNA (rRNA) transcription, processing, and ribosome assembly to form three sub-compartments with different compositions and material properties [8,9]. This organization is thought to facilitate the vectorial expulsion of ribosomes through and out of the nucleolus [10,11]. In most eukaryotic nuclei, the nucleolus is surrounded by Pericentromeric Heterochromatin (PCH), a chromatin compartment composed of megabases of pericentromeric repeats, including tandemly repeated satellite DNA and transposable elements[12,13]. PCH is associated with transcriptional silencing and has essential roles in nuclear architecture, chromosome segregation, and genome stability [14]. Under the microscope, PCH can be visualized as chromatin regions enriched for the AT-rich DNA dye DAPI, histone modifications di- and tri-methylation of histone H3 (H3K9me2/3), and the cognate epigenetic reader Heterochromatin Protein 1 (HP1) [15]. HP1 is a multivalent protein with structured and disordered domains [16] that phase separates and partitions DNA and nucleosomes *in vitro* [17,18], and forms a liquid-like condensate nucleated by H3K9me2/3 enriched chromatin *in vivo* [19–21]. One explanation for why the nucleolus is adjacent to PCH is that tandem repeats of rDNA are positioned next to heterochromatic satellite repeats on a subset of chromosomes [22]. However, cytological and sequencing analyses have revealed that sequences from most chromosomes (including those lacking rDNA) make contacts with the nucleolus [23–25], suggesting that cis-proximity to rDNA is not necessary for PCH to organize at the nucleolar edge. The mechanisms that position PCH from all chromosomes around the nucleolus are unclear. Understanding this is important, as PCH dissociation from nucleoli

75 in senescent cells suggests a link between PCH-nucleolar association and cellular health
76 [26].

77 In this study, we use live imaging and genetic tools in the *Drosophila melanogaster* model
78 to uncover the dynamic patterns of *de novo* assembly of PCH from all chromosomes
79 around the nucleolus. Removal of rDNA, and thus a functional nucleolus, caused dramatic
80 changes in PCH assembly dynamics and redistribution of some nucleolar proteins into
81 new bodies or 'neocondensates'. These *in vivo* phenotypes led us to develop a physical
82 model based on a hierarchy of interaction strengths between PCH, nucleoli, and
83 'amphiphilic' protein(s) able to interact with both nucleolar and PCH components.
84 Simulations recapitulated the layered organization of nucleoli and PCH, as well as the
85 phenotypes caused by rDNA deletion. Importantly, this model was validated by
86 demonstrating that Pitchoune, a DEAD-box RNA-Helicase protein, acts as an amphiphilic
87 linker responsible for PCH-nucleolar associations. We propose that disrupting affinity
88 hierarchies between interacting condensates can redistribute their constituents to form
89 neocondensates or other aberrant structures that may result in cellular disease
90 phenotypes.

91 **Results**

92 **Dynamic conformational changes during assembly of PCH around the nucleolus**
93 **during *Drosophila* embryonic development**

94 As in other eukaryotes, *Drosophila* nucleoli are multi-layered [9,27], with the outermost layer
95 Granular Component (GC) marked by Modulo (the fly ortholog of Nucleolin) and the
96 Dense Fibrillar Component (DFC) marked by Fibrillarin. Live imaging in late embryos
97 (~12-16 hr, Embryonic Stage 14-16) co-expressing fluorescently tagged transgenes of
98 Fibrillarin or Modulo along with HP1a, shows that HP1a is positioned around the GC at
99 the apical edge of the nucleus (**Fig. 1a, Extended Data Fig. 1a).** In the canonical
100 'surrounded' conformation, HP1a does not fully engulf the nucleolus but organizes around
101 its lateral sides, covering ~30% of the nucleolar surface in 3D (**Supplementary Movie 1**).
102 This surrounded conformation persists through development, as observed in gut cells in
103 late embryos, epidermal cells in first instar larvae, and eye discs in third instar larvae
104 (**Extended Data Fig. 1b)**.

105 To determine how PCH forms the surrounded conformation around the nucleolus, we
106 performed high-resolution time-lapse imaging of HP1a and Fibrillarin in early *Drosophila*
107 embryos. *Drosophila* embryos undergo 14 syncytial nuclear divisions before
108 cellularization at the blastoderm stage, with chromatin features such as H3K9 methylation
109 progressively established during these cycles [28]. PCH condensates first emerge in cycle
110 11 [19] while nucleoli first emerge in cycle 13 [29], making cycle 13 the earliest time both
111 condensates appear in the same nucleus. Upon entry into cycle 13 interphase, HP1a and
112 Fibrillarin proteins are initially diffuse throughout the nucleus, then within ~8 mins, each

113 becomes enriched in multiple, distinct foci (**Fig. 1b(i) and Supplementary Movie 2**).
114 Small PCH and nucleolar condensates remain separated throughout cycle 13, likely
115 because growth is limited by the short interphase (~15 mins) before both dissolve in
116 mitosis [19,29]. Cycle 14 begins like cycle 13 in that HP1a and Fibrillarin foci emerge soon
117 after mitotic exit and are initially separated. During the longer interphase (90 min) of cycle
118 14, PCH and nucleoli undergo extensive growth in volume and self-fusions [19,21,29].
119 However, instead of forming the canonical surrounded conformation, PCH extends away
120 from the nucleolus while being tethered to the nucleolus at one end, hereafter referred to
121 as the 'extended conformation' (**Fig. 1b(ii) and Supplementary Movie 3**). The extended
122 conformation is also observed in nuclei with two nucleoli, which appear when the two
123 rDNA arrays in a nucleus are unpaired (**Extended Data Fig. 1c**).

124 Continued live imaging of HP1a and Fibrillarin in post-blastoderm, asynchronous cell
125 divisions revealed how the extended PCH configuration dynamically transitions into the
126 surrounded form observed in later developmental stages. PCH rapidly forms the extended
127 configuration by lining the nuclear edge through the rest of cycle 15 (**Fig. 1b(iii) and
128 Supplementary Movie 4**), transitions between the extended and surrounded
129 configurations during cycle 16 (**Fig. 1b(iv) and Supplementary Movie 5**) and stably
130 wraps around the nucleolus ~15 min into cycle 17 interphase (**Fig. 1b(v) and
131 Supplementary Movie 6**). HP1a occupancy around the nucleolus increases from 10%
132 to 30% in 3D between cycles 14 and 17 (**Fig. 1c**). HP1a reorganization observed in Cycle
133 17 is mirrored in cultured S2 cells exiting mitosis, where HP1a transitions through an
134 'extended' intermediate before stably surrounding the nucleolus (**Extended Data Fig. 1d**).

135 Next, we performed DNA FISH for pericentromeric repeats and rDNA to determine how
136 PCH and nucleolar DNA sequences are reorganized in 3D during development. In the
137 early embryo, PCH is connected to the nucleolus due to the physical proximity of rDNA
138 repeats to pericentromeric repeats on the X and Y chromosomes in both females (XX)
139 and males (XY) (**Extended Data Fig. 2a-b**). In the late embryo, we observed an intense
140 rDNA signal at the nucleolar periphery, adjacent to the 359bp sequence on the X
141 chromosome (**Extended Data Fig. 2c**). This is consistent with the process of nucleolar
142 dominance, where the rDNA array on one X chromosome is silenced in *Drosophila*
143 *melanogaster* [30,31], and with the repositioning of silent rDNA outside the nucleolus [32]. The
144 1.686 repeat sequences, located on chromosomes lacking rDNA (chromosomes 2 and
145 3), are positioned away from the nucleolus during cycle 15 (Stage 8), forming the
146 'extended conformation', but relocate to the nucleolar edge in the late embryo (**Extended
147 Data Fig. 2d-e**). Immunostaining early embryos for H3K9me2/3, Lamin, and Fibrillarin
148 reveals that the PCH lines the nuclear lamina in the 'extended conformation' (**Fig. 1d**).

149 Together, these experiments detail the reorganization of the two largest biomolecular
150 condensates during *Drosophila* embryonic development at high spatial and temporal
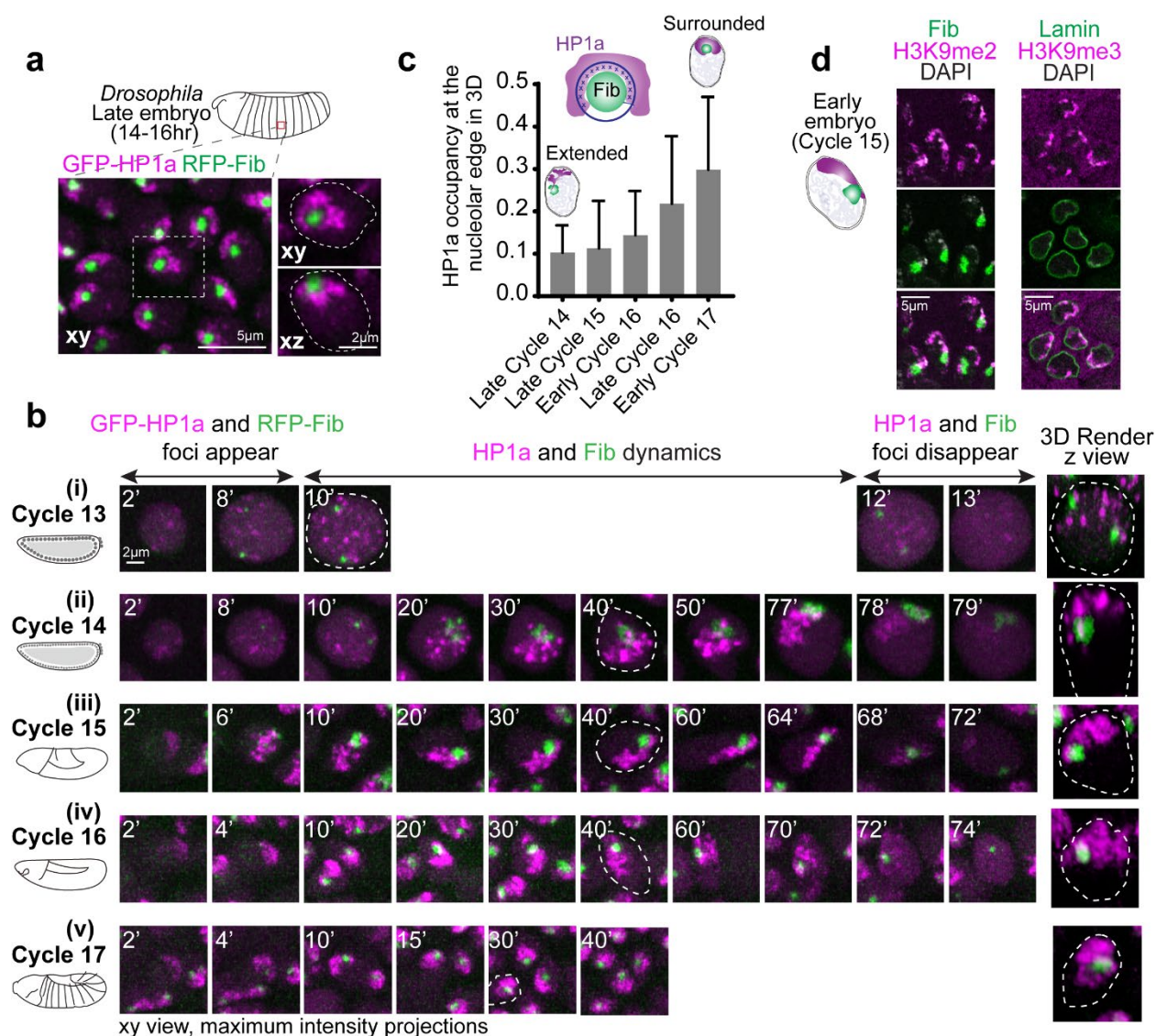151 resolution. We observe that PCH and nucleolar condensates undergo independent

Fig. 1: PCH is reorganized during *Drosophila* embryonic development from extended away to positioned around the nucleolus. (**a**) Maximum intensity projections showing the distribution of GFP-HP1a (magenta) and RFP-Fibrillarin (green) in live epidermal nuclei from a late-stage *Drosophila* embryo (Stage 16, ~14-16hr). The nucleus outlined by the white dashed box is magnified on the right, presenting xy and xz views with white dashed lines indicating the nuclear boundary. (**b**) Maximum intensity projections (xy view) of individual live nuclei of GFP-HP1a (magenta) and RFP-Fibrillarin (green) localization in Cycles 13-17 of *Drosophila* embryogenesis. The numbers on the top left corner of each image indicate time (in minutes) after mitotic exit. The 3D render of the nucleus marked with white dashed lines is presented (not to scale) at the right end of the panel. (**c**) Quantification of HP1a occupancy at the nucleolar edge during specific developmental cycles. "Early Cycle" refers to nuclei between 15-30 mins into the specified interphase, "Late Cycle" refers to nuclei between 50-70 mins. Schematic above the graph illustrates the approach used to calculate the fraction of the nucleolar edge (dark blue shell) intersecting with HP1a (dark blue crosses). Bar graphs represent mean with s.d. n>50 nuclei (from 5 embryos) at each time point. (**d**) Immunofluorescence staining of nuclei from early (Cycle 15) embryos. Left: H3K9me2 (magenta) and Fibrillarin (green). Right: H3K9me3 (magenta) and Lamin (green).

152 nucleation, growth, and fusion, displaying cycle-specific differences while dynamically
153 transitioning from the extended (predominantly nuclear periphery associated) to the
154 surrounded configurations (nucleoli associated) (summarized in **Extended Data Fig. 2f**).

155 **Embryos lacking nucleoli display increased PCH compaction and neocondensate**
156 **formation**

157 The specific patterns of PCH reorganization around the nucleolus during embryonic
158 development prompted us to ask if the nucleolus impacts PCH assembly dynamics. We
159 imaged RFP-HP1a and GFP-Fib in embryos that lack any rDNA repeats (designated
160 hereafter as -rDNA) due to a rearranged X chromosome (C(1)DX/0). No functional
161 nucleoli are formed in -rDNA embryos [29], but they develop through early embryogenesis
162 due to maternal deposition of ribosomes. Fibrillarin forms spherical structures (as
163 previously reported by Falahati et al. 2016 [29]), which are located at a significantly longer
164 distance from the HP1a/PCH condensate compared to their distance in wildtype (+rDNA)
165 controls (**Fig. 2a-b;** +rDNA mean=1.78μm, -rDNA mean=3.69μm, p<0.0001). This result
166 suggests that Fibrillarin and HP1a proteins do not interact directly. Instead, when factors
167 responsible for nucleolus formation (rDNA/rRNA) are not present, Fibrillarin self-
168 associations [33] and/or secondary affinities with other structures or molecules are sufficient
169 to cause the formation of new enrichments (hereafter termed 'neocondensates') not found
170 in wildtype cells. The 'extended' HP1a conformation typically observed in cycles 14 and
171 15 is replaced by a collapsed, rounded structure at the apical end of -rDNA nuclei (**Fig.**
172 **2a, c**). The aspect ratio (major axis/minor axis) of the HP1a domain is significantly
173 reduced (**Fig. 2d**; +rDNA mean=1.96, -rDNA mean=1.40, p<0.0001). Additionally, the
174 distance between pericentromeric repeats 1.686 (on Chr 2 and 3) and AAGAG (satellite
175 repeats on all chromosomes) is decreased in -rDNA nuclei compared to +rDNA controls
176 (**Fig. 2e-f**; +rDNA mean=0.74μm, -rDNA mean=0.32μm, p<0.0001). Thus, PCH loses the
177 extended configuration and shows increased compaction in the absence of
178 rDNA/nucleoli, where compaction is defined by the reduction in 3D space between PCH
179 elements.

180 To our surprise, PCH transitioned to a toroidal (donut-like) structure in all imaged cells in
181 late-stage -rDNA *Drosophila* embryos, with a core devoid of HP1a ('PCH void') (**Fig. 3a**).
182 We visualized this transition at increased spatial resolution in the large nuclei of the
183 amnioserosa, which forms a monolayer on the dorsal surface of the embryo during
184 gastrulation [34] (**Fig. 3b-c and Supplementary Movie 7**). In addition to the absence of
185 HP1a, the PCH void also lacked the major nucleolar proteins Fibrillarin (**Fig. 3c**), which
186 formed a separate neocondensate, and Modulo, which dispersed in the nuclear space
187 (**Extended Data Fig. 3a**). The PCH void did not contain DNA (DAPI staining), histones
188 marked with H3K9me2 (IF) (**Extended Data Fig. 3c**), or any significant accumulation of
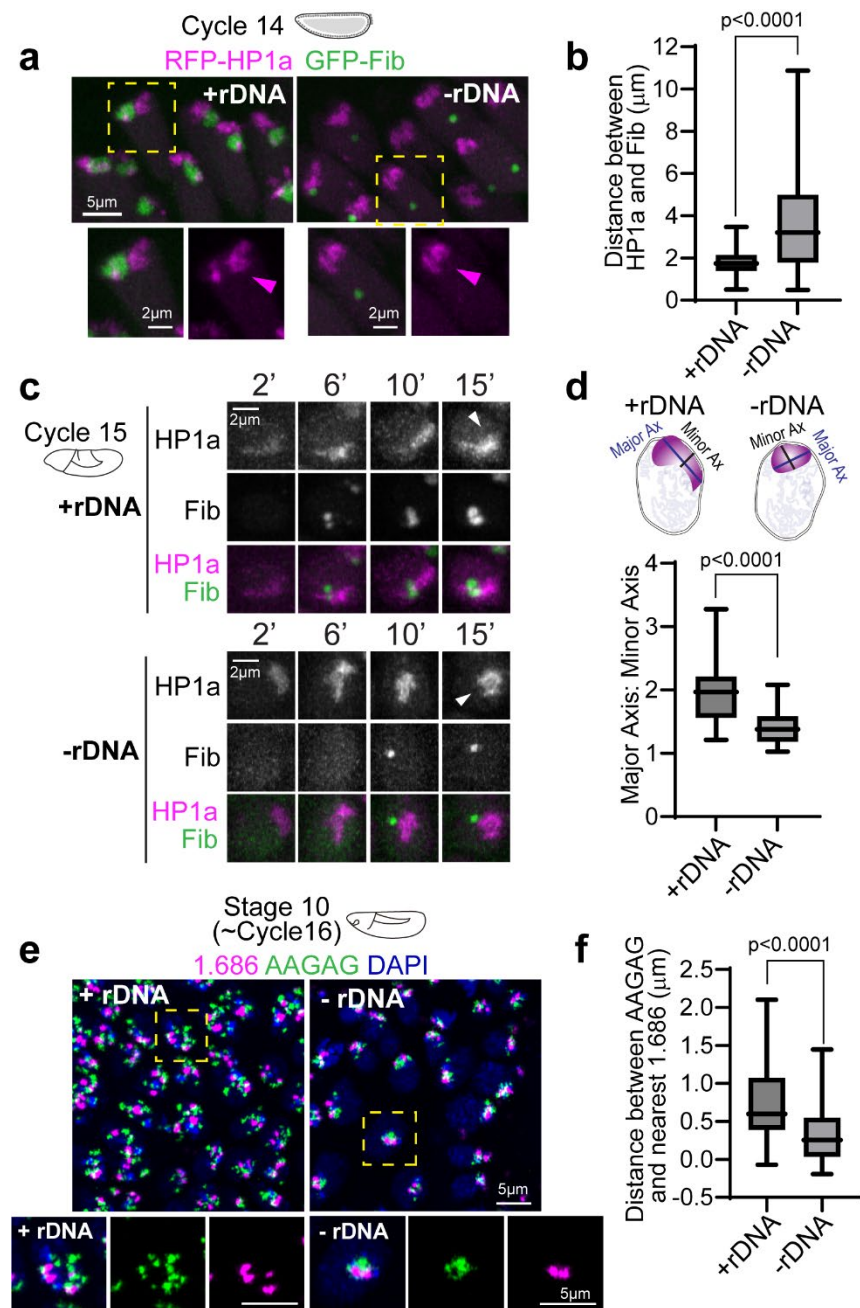189 RNAs (Propidium Iodide staining) (**Extended Data Fig. 3d**). However, treatment with 488

6

Fig. 2: Increased PCH compaction in embryos lacking rDNA. (**a**) Maximum intensity projections of live nuclei from wildtype embryos (+rDNA) and mutant embryos lacking rDNA (-rDNA) at Cycle 14, expressing RFP-HP1a (magenta) and GFP-Fibrillarin (green). The dashed yellow box highlights the nucleus enlarged in the panel below. (**b**) Distance between the centers of geometry of HP1a and Fibrillarin in +rDNA and -rDNA embryos. n>200 nuclei (from 5 embryos) for each genotype. (**c**) Maximum intensity projections from live imaging of nuclei from +rDNA and -rDNA embryos showing the reassembly of RFP-HP1a (magenta) and GFP-Fibrillarin (green) at the indicated minutes after the start of Cycle 15. White arrowheads point to HP1a organization 15 minutes after the start of Cycle 15 in +rDNA and -rDNA embryos. (**d**) Quantification of the aspect ratio (major axis over minor axis) of HP1a segments 15 minutes after the start of Cycle 15 in +rDNA and -rDNA embryos. n>30 nuclei in each genotype. (**e**) Maximum intensity projections of FISH (Fluorescence in Situ Hybridization) of satellite repeats 1.686 (magenta) and AAGAG (green) in DAPI (blue)-stained nuclei in +rDNA and -rDNA Stage 10 embryos. The dashed boxes mark the nuclei enlarged on the right. (**f**) Quantification of the distance between AAGAG and its nearest 1.686 locus. n>40 pairs of loci in each genotype. Box plots extend from 25th to 75th percentile. Error bars: Min to Max.
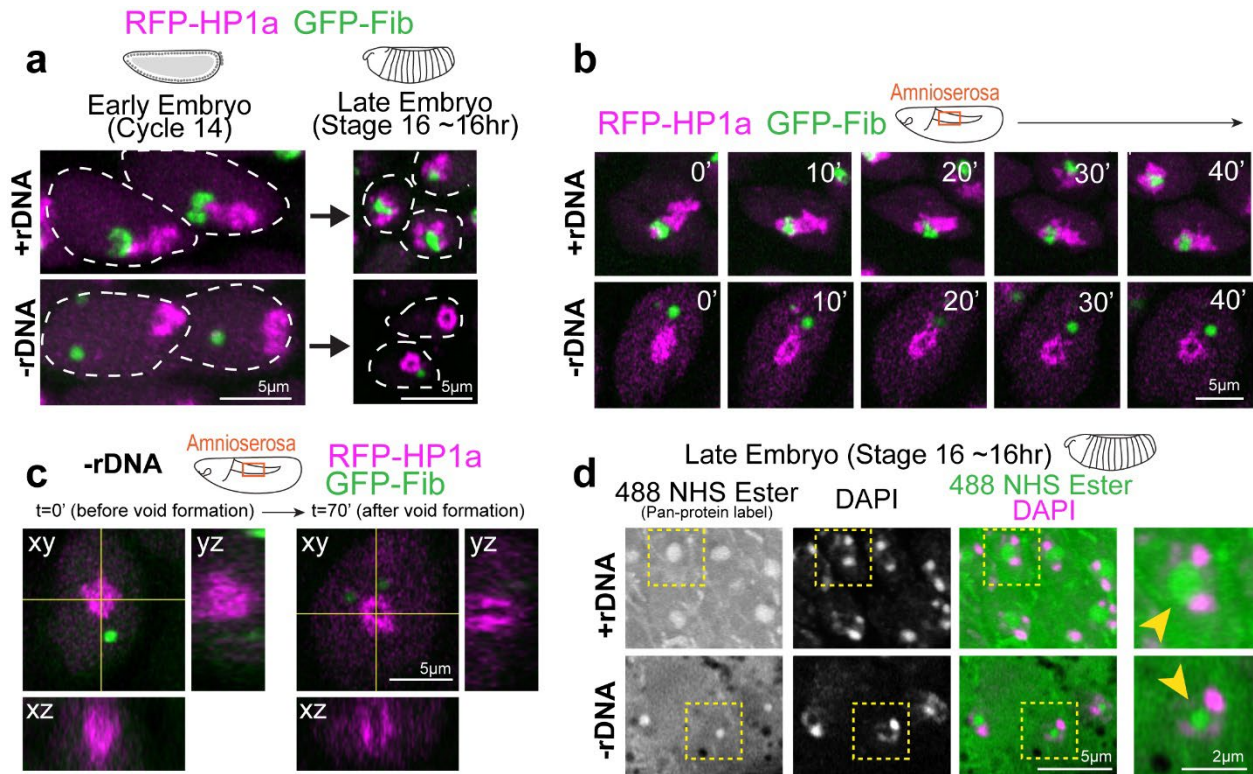
Fig. 3: A protein-filled core reshapes the PCH condensate to a toroid-like structure in -rDNA developing embryos. (**a**) Representative stills of live +rDNA and -rDNA nuclei at Cycle 14 and in Stage 16 (late stage) embryos showing RFP-HP1a (magenta) and GFP-Fibrillarin (green). (**b**) Time-lapse stills (single slices) of a +rDNA and -rDNA amnioserosa nucleus with HP1a (magenta) and Fibrillarin (green). T=0 mins was set to capture the time window where PCH transitions from a compacted to a toroidal structure in -rDNA amnioserosa nuclei. (**c**) Orthogonal projections along yellow intersecting lines in an amnioserosa nucleus from a -rDNA embryo before and after the formation of the 'PCH void'. (**d**) Late embryos (Stage 16) with the +rDNA or -rDNA genotype co-stained with a pan-protein label, 488 NHS Ester (green), and DAPI (magenta) show that the 'PCH void' in -rDNA embryos is enriched for proteins (yellow arrowhead). Nuclei marked with the yellow dashed box are enlarged on the right.

190   NHS Ester, a pan-protein label [35], revealed that the PCH void was enriched for proteins
191   (**Fig. 3d**).

192   We conclude that PCH initially displays an atypical, compacted morphology in embryos
193   lacking rDNA and nucleoli. As development proceeds, the PCH morphs into an abnormal
194   toroidal structure whose central core (the PCH void) lacks HP1a, nucleolar proteins,
195   chromatin, and RNA but is filled with protein(s) that may represent another
196   neocondensate. Together, these results reveal that nucleoli are required to organize PCH
197   in the 3D nuclear space by preventing PCH hyper-compaction and that disrupting
198   interactions within or between condensates can create new nuclear structures.

199   **Coarse-grained modeling recapitulates *in vivo* PCH-nucleolar organization**
200   **phenotypes and highlights a potential role for amphiphilic proteins in mediating**
201   **their association**

202   Since the nucleolus and PCH assemble via phase separation or similar mechanisms
203   [8,19,21,36], we drew inspiration from the physical theory of three-phase wetting to better
204   understand PCH-nucleolar organization in the nucleoplasm. This theory states that an
205   equilibrium between the interfacial tensions (i.e., the energetic cost of forming an interface
206   between two phases) determines the spatial configurations of the different phases [37] (**Fig.**
207   **4a**, fully engulfing, partial engulfing, or individual separated phases). These interfacial
208   tensions are dictated by the relative interaction strengths between the components of the
209   different phases. To describe the different three-phase spatial configurations we
210   introduced the spreading coefficient of a phase i, S_i,

211
$$S_i = \gamma_{jk} - \left(\gamma_{ij} + \gamma_{ik}\right)$$

212   where the letters $i, j,$ and k, represent three different phases, γ_{jk} is the interfacial tension
213   between phases j and k, γ_{ij} is the interfacial tension between phases i and j, and γ_{ik} is
214   the interfacial tension between phases i and k. For every three-phase combination, there
215   are three spreading coefficients, and depending on whether such spreading coefficients
216   are positive or negative, different spatial configurations are attained [37]. We exemplify this
217   using PCH (H), the outermost nucleolar layer GC (G), and the nucleoplasm (N) (**Fig. 4a**).

218   To connect the theory of wetting with our *in vivo* results, we used a minimal coarse-grained
219   model that incorporates the molecular interactions and biophysical parameters that could
220   mediate nucleolar-PCH spatial organization with four minimal components (**Fig. 4b**). (i)
221   PCH (H) as a long, self-attracting polymer. (ii) Fibrillarin (F), which represents a self-
222   associating nucleolar protein. (iii) rDNA (rD) as a polymeric block within the chromatin
223   fiber that experiences good solvent conditions and is flanked by two PCH blocks. Although
224   we do not explicitly account for the presence of rRNA, we use rDNA as a proxy for the
225   nucleating site for Fibrillarin condensates. Finally, (iv) Protein (X), as a self-associating
226   molecule with an affinity for PCH. These properties were attributed to protein X to account

227 for the spherical protein-rich compartment that consistently formed within the PCH-void
228 in -rDNA nuclei (**Fig. 3d**). We then considered what additional properties Protein X could
229 possess to form the observed *in vivo* organization of the nucleolus and PCH.

230 To recapitulate the layered PCH-nucleolar organization, we reasoned the self-
231 associations of Fibrillarin must be stronger than those of protein X, which in turn must be
232 stronger than the self-interactions of PCH. These self-interaction choices result in the
233 following hierarchy of interfacial tensions $\gamma_{FN} > \gamma_{XN} > \gamma_{HN}$, where γ_{iN} is the interfacial
234 tension between a phase enriched in component $i = F, X, H$ and the nucleoplasm (N).
235 Additionally, we note that for a stable association between PCH and the Fibrillarin-rich
236 phase, Protein X must also have an affinity for Fibrillarin (or more generally for nucleolar
237 components), which *in vivo* might be mediated by the presence of rRNA. Therefore, we
238 define Protein X as an 'amphiphilic protein', due to its dual affinity for the PCH and
239 nucleolar phases, as defined previously for synthetic co-condensates [38]. Altogether, these
240 considerations led us to define a hierarchy of interaction strengths (rD-F ≥ F-F > X-X > F-
241 X > X-H > H-H) as an initial set of parameters listed in the 4x4 interaction matrix (**Fig. 4c**).
242 Simulating this affinity hierarchy recapitulated the canonical PCH-nucleolar organization
243 observed in +rDNA animals *in vivo* (**Fig. 4c and Supplementary Movie 8**). Various
244 scenarios incompatible with the experimental observations of the layered organization of
245 the nucleolus and PCH arise by deviating from the hierarchy of self-interaction strengths
246 in the simulations. For example, instead of having a complete engulfing of the nucleolus
247 by PCH, there are partial engulfing or no engulfing scenarios when the interaction
248 between the amphiphilic proteins is larger than that of Fibrillarin (**Extended Data Fig. 4d**).
249 Importantly, our choice of interaction parameters is not unique as long as the interfacial
250 tensions fulfill $\gamma_{FN} > \gamma_{XN} > \gamma_{HN}$, we obtain a complete engulfing of the nucleolus by PCH.
251 A detailed rationale for the choice of parameters is described in the Methods section.

252 Next, we modeled the consequences of removing rDNA by setting the rDNA-Fibrillarin
253 interactions to zero, thus eliminating its ability to recruit nucleolar components such as
254 Fibrillarin and X. Reducing the attraction between Fibrillarin and the amphiphilic protein
255 X, which increases the interfacial tension between the Fibrillarin-rich and the amphiphilic-
256 rich phases, γ_{FX}, resulted in the formation of a protein X neocondensate within the PCH
257 void and a spatially separated Fibrillarin neocondensate (**Fig. 4d-e**), as observed in
258 -rDNA embryos *in vivo* (Fig. 2 and 3). These phenotypes are observed in simulations
259 whenever the protein X – PCH interaction strength is greater than or equal to the X –
260 Fibrillarin interactions (i.e., X-H ≥ F-X) (**Extended Data Fig. 4e-f**). In the model, the
261 nucleation of the new phase of amphiphilic protein X occurs within the PCH to reduce the
262 cost of creating an interface of protein X with the solvent. Instead, being surrounded by
263 PCH can reduce this interfacial energy, as expected from a wetting picture of simple
264 liquids [37]. We conclude that incorporating affinity hierarchies and an amphiphilic protein
265 X into a minimal model recapitulates the observed *in vivo* organization of PCH and
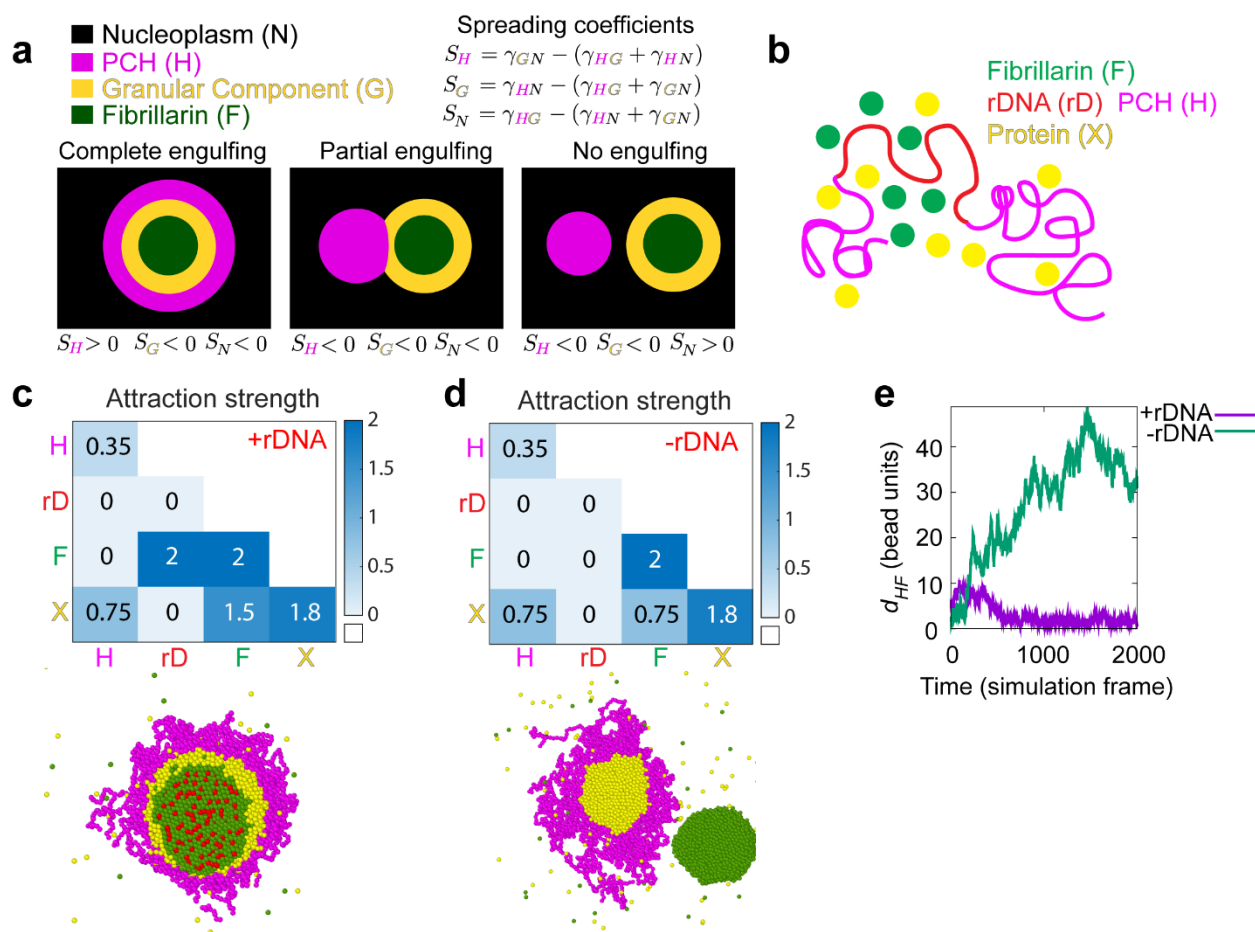
Fig. 4: A hierarchy of interaction strengths between PCH, nucleoli and 'amphiphilic' protein(s) recapitulates their +rDNA and -rDNA *in vivo* organization. (**a**) The schematic shows the spatial organization of three different phases. The interfacial tensions, γ_{ij}, between phases *i* and *j* (where *i* and *j* can be nucleoplasm (N) in black, PCH (H) in magenta, or the granular component (G) in yellow) are used to define the spreading coefficients, S_i, shown in the top right corner. Given the assumption that $\gamma_{GN} > \gamma_{HN}$, the three possible combinations of spreading coefficients determine the configuration of the three phases, ranging from complete engulfing to partial engulfing to no engulfing. Since the Fibrillarin-rich phase (F) is always within a functional nucleolus, its spreading coefficients are not included in this analysis. (**b**) Course-grained modelling of nucleolar-PCH assembly with four minimal components: PCH (H) as a self-interacting polymer (magenta) rDNA (rD) as polymeric block embedded within PCH (red), Fibrillarin (F) as a representative of a self-associating nucleolar protein (green), and a self-associating protein 'X' (yellow) representing those enriched in the PCH void in -rDNA nuclei. (**c** and **d**) The matrices indicate the strengths of interaction (blue gradient, units: k_BT) between Fibrillarin (F) (green), rDNA (rD) (red), PCH (H) (magenta), and protein (X) (yellow), which has dual affinities for both H and F. The indicated affinity hierarchies result in simulated outcomes that recapitulate their +rDNA and -rDNA organization observed *in vivo*. (**e**) Distance (d_{HF}) between the centers of mass of PCH (H) and Fibrillarin (F) clusters in +rDNA and -rDNA simulations.

11

266 nucleolar condensates in both +rDNA and -rDNA conditions. This led us to predict that in
267 WT conditions, protein X would be a self-associating protein with dual affinities for the
268 nucleolus and PCH, albeit with a weaker affinity for PCH components (F-X > X-H).

The DEAD-box RNA Helicase Pitchoune is a granular compartment protein that forms a neocondensate within PCH in -rDNA embryos

271 A candidate for an amphiphilic protein that can interact with both PCH and the nucleolus
272 emerged from Falahati et al., 2017 [36]. They reported that the DEAD-box RNA helicase
273 Pitchoune (Pit), typically a granular component (GC) nucleolar protein [39], mislocalized to
274 the apical part of the nucleus in cycle 14 -rDNA embryos, similar to the compacted PCH
275 domain observed in our studies (Fig. 2a). Pitchoune, the *Drosophila* ortholog of DDX18,
276 is required for larval development [39], and possesses an N-terminal intrinsically disordered
277 region (IDR), a central helicase core, and a disordered C-terminal domain (**Fig. 5a**). We
278 identified two tandem "PxVxL" HP1a-interacting motifs [40,41] in the C-terminal tail of
279 Pitchoune with PVVDL being conserved across eukaryotes along with LKVGA being
280 conserved among Drosophilids (**Fig. 5a and Extended Data Fig. 5a**). Additionally,
281 Pitchoune belongs to the DDX family of proteins, other members of which phase separate
282 and modulate condensate behavior [42]. Together, these clues led us to hypothesize that
283 Pitchoune could be a candidate amphiphilic protein that can 1) form condensates and 2)
284 have a dual affinity for both the nucleolus and PCH.

285 Consistent with its role as a GC nucleolar protein [43], Pitchoune is enriched in the
286 outermost nucleolar compartment in *Drosophila* embryos and S2R+ cells (**Fig. 5a**). Next,
287 to investigate whether Pitchoune is enriched in the PCH void in -rDNA embryos, we
288 performed live imaging in +rDNA and -rDNA embryos co-expressing Pit-GFP and RFP-
289 HP1a transgenes. In cycle 14 +rDNA nuclei, Pitchoune localizes to the nucleolus while
290 HP1a is in the extended configuration. In contrast, a faint Pitchoune signal co-localizes
291 with the more compact HP1a domain in -rDNA nuclei (**Fig. 5b**). In cycle 17 epidermal
292 nuclei and amnioserosa nuclei, HP1a surrounds Pitchoune in +rDNA embryos, whereas
293 in -rDNA embryos, high-intensity Pitchoune puncta appear within each compacted HP1a
294 condensate (**Fig. 5b**). Time-lapse imaging of amnioserosa nuclei in -rDNA embryos
295 revealed that Pitchoune is initially faintly mixed but gradually separates from HP1a, with
296 the intensity of Pitchoune increasing ~2.5-fold over an hour (**Fig. 5c-d and
297 Supplementary Movie 9**). Furthermore, the circularity of Pitchoune increases and
298 approaches 1 (in projections) (**Fig. 5e**), and the area of Pitchoune decreases over time
299 (**Fig. 5f**). These results suggest that Pitchoune demixes from HP1a and forms a spherical
300 neo-condensate surrounded by PCH, minimizing interfacial energy by avoiding the
301 creation of a larger energy interface between Pitchoune and the nucleoplasm (**Fig. 5g**).
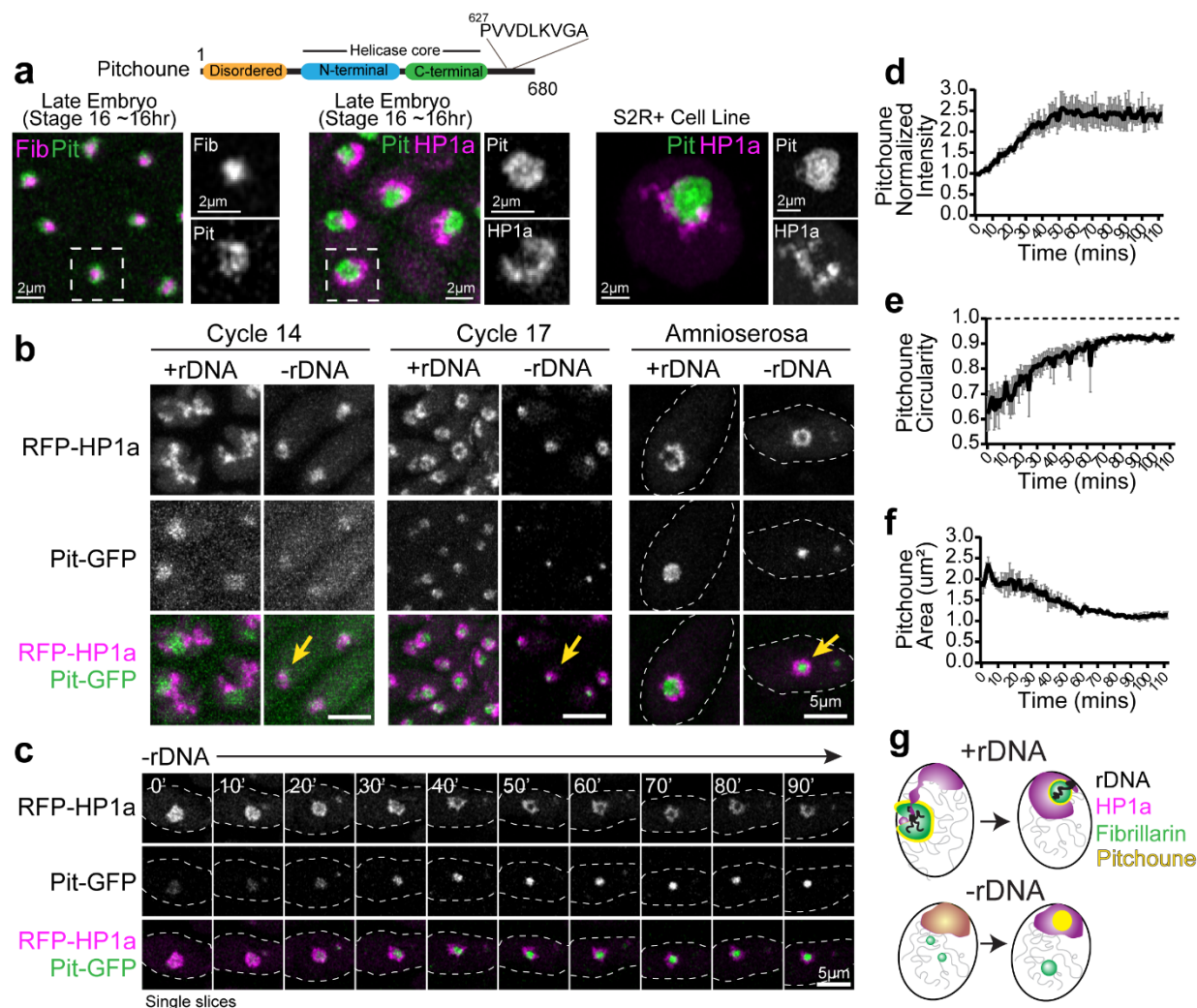
Fig. 5: The RNA Helicase Pitchoune is enriched in the PCH void in -rDNA embryos. (**a**) Protein Subdomains in Pitchoune (Pit) with an N-terminus disordered domain, central helicase core and C-terminus with a conserved HP1a interacting motif. Left to Right: Panels showing the localization of RFP-Fib (magenta) and Pit-GFP (green) in Stage 16 embryo, RFP-HP1a (magenta) and Pit-GFP (green) in Stage 16 embryo, and Scarlet-I-HP1a (magenta) and Pit-mYFP (green) transiently transfected in S2R+ *Drosophila* cells. (**b**) Maximum intensity projections of Cycle 14, Cycle 17 and amnioserosa nuclei from +rDNA and -rDNA embryos showing RFP-HP1a (magenta) and Pit-GFP (green). Yellow arrows in -rDNA in Cycle 17 show the mixing of Pit and HP1a, while yellow arrows in -rDNA in cycle 17 and amnioserosa show the formation of the Pit neocondensate in the PCH void. (**c**) Time-lapse stills (single slices) of a -rDNA amnioserosa nuclei with RFP-HP1a (magenta) and Pit-GFP (green). (**d**) Mean intensity, (**e**) Circularity, and (**f**) Area of projections of Pitchoune in -rDNA embryos in amnioserosa nuclei. Mean of 35-60 nuclei at each time point in n=3 embryos. Error Bars: s.e.m. (**g**) Schematic summarizing nuclear organization phenotypes observed in +rDNA and -rDNA embryos.

13

Pitchoune and its HP1a-interacting motif are required for PCH-nucleolar associations

Supported by our model and *in vivo* imaging, our findings indicate that Pitchoune is a candidate amphiphile between PCH and nucleoli as a granular compartment nucleolar protein with a lower affinity for PCH/HP1a. We next investigated the consequences of removing Pitchoune on PCH-nucleolar associations. If Pitchoune regulates these associations, we predicted that its depletion would disrupt the surrounding configuration. We first tested this by decreasing the concentration of the amphiphilic protein in the physical model while keeping all other parameters the same as in Fig. 4c. The simulations revealed a progressive detachment of PCH from the nucleolus as Pitchoune levels decreased (**Fig. 6a**). Note that in both simulations and *in vivo* experiments, even with the loss of Pitchoune, nucleoli and PCH are expected to maintain a singular attachment at the PCH-embedded rDNA locus. This is in contrast with the separation of Fibrillarin and PCH observed in embryos lacking rDNA (**Fig. 2a, 4c**).

Next, we depleted Pitchoune using RNAi in the female germline (using a maternal GAL4 driver) to assess the impact of Pitchoune knockdown in *Drosophila* embryos. However, ovary development was halted, and no eggs were laid following Pitchoune knockdown in the female germline (**Extended Data Fig. 6a-b**), preventing further assessment of the effects of Pitchoune knockdown in early embryos. These phenotypes align with the growth defects observed in *pitchoune* homozygous mutants that die as small first instar larvae [39], likely surviving early development due to maternal deposits of Pitchoune. Therefore, we used eyeless-GAL4 to knock down Pitchoune in the eye-antennal discs of third-instar larvae. Pitchoune knockdown severely disrupted the normal development of eye-antennal discs (**Extended Data Fig. 6c**). Most importantly, viable cells displayed a 50% reduction in the fraction of the nucleolar edge occupied by H3K9me2 after Pitchoune knockdown (control RNAi mean = 0.296, Pitchoune RNAi mean = 0.146, p-value = 0.0011) (**Fig. 6b-c**).

We also knocked down Pitchoune in S2R+ *Drosophila* cultured cells using RNAi, achieving ~60% reduction in Pitchoune transcripts (**Extended Data Fig. 6d**). As observed in eye discs, Pit knockdown decreased HP1a occupancy at the nucleolar edge and disrupted its organization relative to the nucleolus, with ~50% reduction in HP1a occupancy at the nucleolar edge, and a decrease in the percentage of nuclei displaying the surrounded configuration (Mock RNAi: 87%, Pit RNAi: 27%) (**Fig. 6d-e, Extended Data Fig. 6e-f**). These phenotypes were rescued by reintroducing full-length Pitchoune (**Fig. 6e-f, Extended Data Fig. 6f**). We conclude that Pitchoune is important to establish or maintain the surrounded configuration.
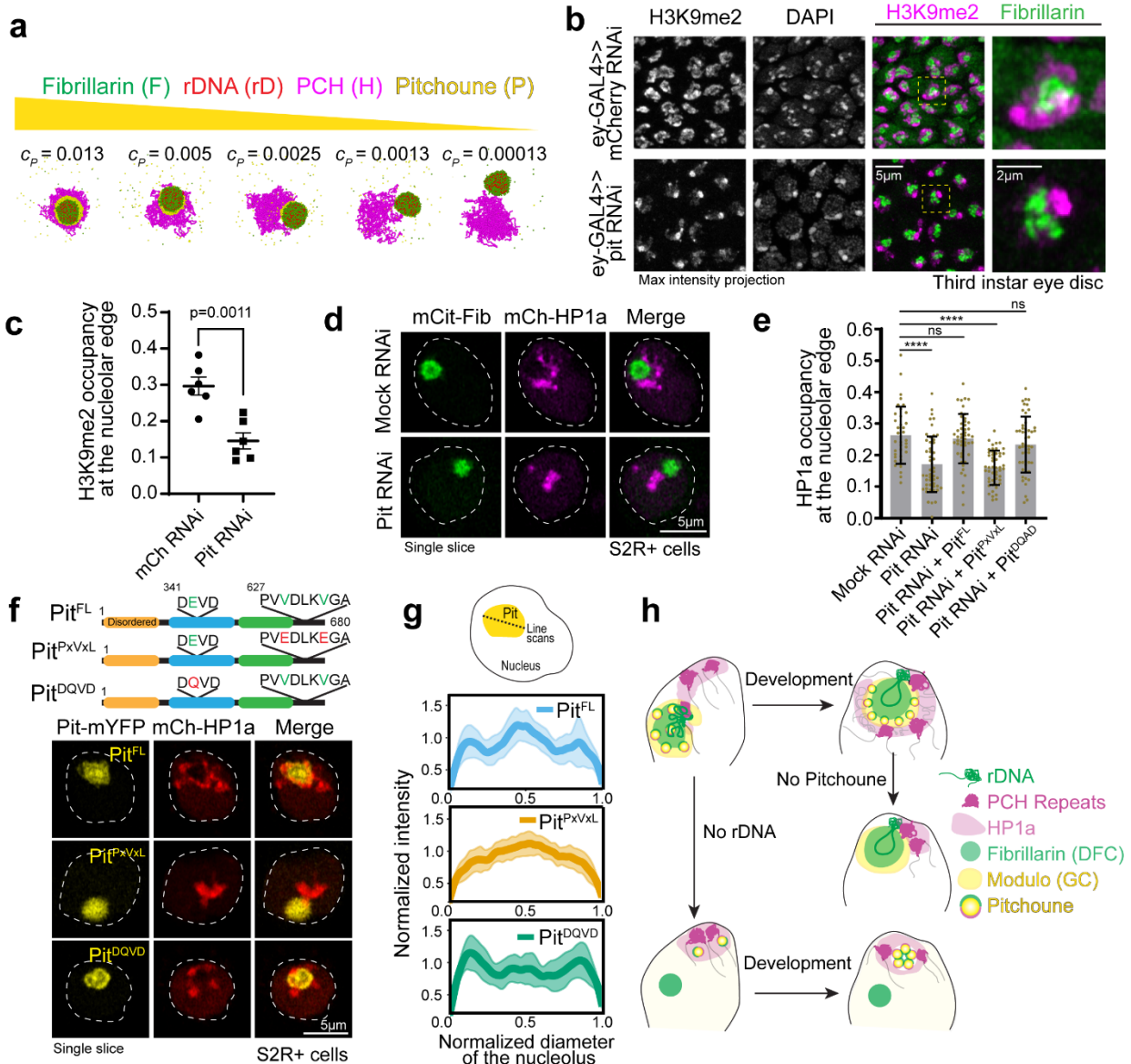
Fig. 6: Knockdown of Pitchoune or mutations in its HP1a-interaction motif disrupt PCH-nucleolar associations. (**a**) Simulation endpoint snapshots demonstrate how decreasing the concentration (c_P) of Pitchoune (P) (yellow) reduces the association of PCH (H) (magenta) around the Fibrillarin condensate (F) (green). (**b**) Immunofluorescence of H3K9me2 (magenta), Fibrillarin (green) and DAPI in nuclei from dissected eye-discs in third instar larvae from UAS-pit RNAi and UAS-mCherry RNAi (control) driven by the eyeless-GAL4 driver. (**c**) Quantification of the fraction of the nucleolar edge occupied by H3K9me2. Each data point indicates the mean value from one animal. n=6 animals with over 500 nuclei in total for each experimental group. Error bars: s.e.m. (**d**) Nuclei expressing Citrine-Fib and mCherry-HP1a transiently transfected after Pitchoune knockdown show decreased association of HP1a from the nucleolus. (**e**) Fraction of the nucleolar edge occupied by HP1a following Pit knockdown and rescue with Full length Pit (Pit^{FL}), Pit^{PxVxL} and Pit^{DQVD}. n=38-50 nuclei for each experimental group. Bar graphs show the mean ± s.d. (**f**) Schematic representation of Pitchoune mutations introduced: Pit^{PxVxL} contains mutations of the central valine (V) to glutamic acid (E) in the conserved PxVxL motifs. The putative helicase mutant is denoted as Pit^{DQVD}. Representative nuclei transfected with Pit^{FL}, Pit^{PxVxL}, and Pit^{DQVD} following RNAi-mediated knockdown of endogenous Pitchoune. (**g**) Line scans show Pitchoune distribution in the nucleolus of cells transfected with Pit^{FL} (n=25), Pit^{PxVxL} (n=37) and Pit^{DQVD} (n=40) after Pit RNAi. Intensities are normalized to the average value for each profile, and lengths are normalized to the diameter of the corresponding nucleolus. Solid line: mean, shaded error region: s.d. (**h**) Model for the organization of PCH (repeats and HP1a) around the nucleolus (rDNA, Fibrillarin and Modulo) via an amphiphilic linker Pitchoune during *Drosophila* development.

338

To determine the molecular basis of Pitchoune's 'amphiphilic' nature and test whether it is directly responsible for PCH-nucleolar associations, we investigated the roles of Pitchoune's conserved motifs in mediating these interactions. We disrupted the putative HP1a-interacting PxVxL motifs by mutating the two central valines (V) to glutamic acid (E) (Pit^{PxVxL}). The central V binds in a hydrophobic pocket at the interface of HP1 dimers, and mutating the hydrophobic V to the charged E residue disrupts their HP1 interaction [40]. We also generated a construct mutating the conserved DEVD motif in the Helicase domain to DQVD (Pit^{DQVD}) to block its Helicase activity [39,44] (**Fig. 6f**). Defects in HP1a organization relative to the nucleolus caused by Pit knockdown in S2R+ cells were rescued by transfection with full-length Pitchoune (Pit^{FL}) and Pit^{DQVD} but not Pit^{PxVxL} (**Fig. 6e-f**). When expressing Pit^{FL} and Pit^{DQVD}, 73% and 62% of nuclei, respectively, exhibited the 'surrounded' PCH-nucleolar organization after Pit knockdown, compared to only 30% of nuclei expressing Pit^{PxVxL} (**Extended Data Fig. 6f**). Additionally, Pit^{PxVxL} showed uniform distribution in the nucleolus, unlike Pit^{FL} and Pit^{DQVD} which were enriched at the nucleolar edges (**Fig. 6f, g**). We conclude that the PxVxL motif regulates Pitchoune's sub-nucleolar distribution by promoting its enrichment at the nucleolar-PCH interface. Together, these experiments reveal the molecular basis of Pitchoune's amphiphilic function, showing that it promotes PCH-nucleolar associations through interactions with HP1a via its PxVxL motif.

Discussion

This study presents four main findings on the organization of PCH and nucleoli (**Fig. 6h**): (**1**) During early embryonic development, PCH-nucleolar associations are highly dynamic, transitioning from extended (nuclear edge-associated) to surrounded (nucleolar edge-associated) configurations (**Fig. 1**). (**2**) The nucleolus organizes PCH components in the 3D nuclear space, preventing PCH hyper-compaction (**Fig. 2**). (**3**) A hierarchy of interaction strengths between nucleolar and PCH components, including amphiphilic proteins with affinities for both, recapitulates the spatial organization seen in cells with and without nucleoli, and disrupting these hierarchies generates neo-condensates (**Fig. 3-5**). (**4**) Pitchoune and its C-terminal HP1a binding PxVxL motif are required for normal PCH-nucleolar associations (**Fig. 6**).

Sequence-based approaches have revealed that nuclear organization transitions from a naïve state to specific higher-order patterns during embryonic development [45]. However, these methods typically exclude the highly repetitive sequences that comprise most of the PCH and nucleoli, limiting our understanding of how PCH-nucleoli organization is established during development. Our study addresses this gap by visualizing PCH and nucleolar dynamics during *Drosophila* embryonic development in single nuclei at minute-scale resolution. Initially, PCH from different chromosomes undergo liquid-like fusions [19,21] to form a contiguous condensate that wraps around the nucleolus, explaining how PCH from chromosomes without rRNA genes is also positioned at the nucleolar edge. After

16

378 fusing into a contiguous condensate, PCH remains dynamic, transitioning from an
379 'extended' configuration in cycle 14 to a stable 'surrounded' state around the nucleolus in
380 cycle 17. Transitions in heterochromatin organization reminiscent of the 'extended'
381 intermediate have been observed during early embryonic development in *C. elegans* [46]
382 and mice [47], suggesting similarities across species.

383 In its 'extended' intermediate state, PCH associates closely with the nuclear edge before
384 repositioning around the nucleolus. This finding is intriguing because sequencing-based
385 approaches have shown overlap between Nucleolus Associated Domains (NADs) and
386 Lamin-Associated Domains (LADs) [24,48]. The molecular mechanisms behind this
387 repositioning are unknown, but we speculate that PCH's affinity for the nuclear periphery
388 decreases while its interaction strength with the nucleolus increases between cycles 14
389 and 17, with Pitchoune playing a crucial role. Post-translational modifications or increased
390 concentrations of Pitchoune in cycle 17 might enhance its affinity for HP1a, correlating
391 temporally with the stable surrounding of the nucleolus by HP1a in +rDNA and the
392 appearance of the Pitchoune neo-condensate in -rDNA. Alternatively, the reduction in
393 nuclear size during these developmental stages might cause a crowding effect, bringing
394 PCH closer to the nucleolus. Changes in the volumes or molecular compositions of PCH
395 and nucleolar condensates could also alter relative affinities or biophysical properties
396 such as surface tension and viscosity. Future studies will reveal whether one or more of
397 these mechanisms mediate the dynamic transitions in PCH-nucleolar association during
398 early development.

399 An unexpected finding in this study was the reorganization of compacted heterochromatin
400 into a toroid-like structure, with Pitchoune filling the core when rDNA was removed. This
401 observation led us to propose the amphiphilic model of PCH-nucleolar organization.
402 Pitchoune is a GC-localizing RNA helicase[39,43], has nucleolar localization signal motifs in
403 its N-terminal tail [49], and its yeast ortholog is a ribosome assembly factor [50], altogether
404 highlighting its dominant nucleolar affinity. We define Pitchoune's function as an
405 amphiphile by demonstrating two key points: (i) it forms neo-condensates in the absence
406 of rDNA, indicating self-association, and (ii) while Pitchoune does not stably mix with
407 HP1a, it consistently shares an interface with HP1a in both its normal and neo-
408 condensate forms suggesting a weak affinity for HP1a. This proximity is lost when the
409 HP1a-interacting C-terminal PxVxL motif in Pitchoune is mutated. This gradient in
410 interaction strengths creates a hierarchical organization and stabilizes PCH-nucleolar
411 associations. Such a layering mechanism is distinct from the formation of nested
412 subcompartments within the nucleolus, which are immiscible but associate due to
413 sequential rRNA synthesis, processing and ribosome assembly [8,9,11], however rRNA
414 synthesis doesn't seem to be required for Pit-HP1a associations. While synthetic
415 amphiphiles have been shown to generate multiphasic condensates both *in vitro* [38] and
416 *in vivo* within stress granules [51], we demonstrate this mechanism in a natural context with

417 PCH and nucleoli and propose a generalizable role for amphiphilic molecules in co-
418 organizing immiscible condensates in cells.

419 How does Pitchoune compare to other molecules required for PCH clustering around the
420 nucleolus? For instance, depleting the Nucleoplasmin homolog NLP, CTCF, or Modulo in
421 *Drosophila* cultured cells [52] or NPM1 in human and mouse cell lines [53] causes the loss of
422 heterochromatin clustering around the nucleolar periphery. However, it is unclear if these
423 proteins play a direct role in PCH-nucleolar interactions or are required to form an intact
424 granular component that recruits other key factors. Similarly, loss of the surrounded
425 configuration upon depletion of Pitchoune protein in cultured cells or larval eye discs could
426 result from disrupting the composition or function of the granular component. However,
427 mutating only the key residues in Pitchoune's HP1a binding motif is sufficient to dissociate
428 PCH from the nucleolus, demonstrating that Pitchoune is directly responsible for binding
429 to HP1a and necessary for PCH-nucleolar associations. Nevertheless, a network of
430 structural and regulatory molecules may contribute to Pitchoune localization and the
431 overall affinity of PCH to the nucleolar edge. Proximity ligation or similar methods for
432 identifying a complete set of molecules enriched at the PCH-nucleolar interface will help
433 generate a full understanding of how Pitchoune promotes PCH associations and what
434 regulates the dramatic architectural changes in early development.

435 The composition of condensates is determined by the multivalency and binding affinities
436 of constituent molecules, and hierarchies in these properties can generate the higher-
437 order structure of multi-layered condensates [54,55]. Our findings demonstrate how
438 disrupting condensate nucleation sites or interaction hierarchies can form new, abnormal
439 nuclear structures or 'neocondensates' through inherent self-associations or secondary
440 interactions with other molecules. For example, loss of the nucleolus due to rDNA deletion
441 leads to PCH compaction, which resembles a collapsed polymer, likely due to increased
442 heterochromatin self-interactions. The specific responses of different components to
443 disruption likely reflect the types and relative strengths of their encoded interaction
444 modules. For instance, when rDNA is removed, Modulo is broadly dispersed throughout
445 the nuclear volume, likely due to its lack of self-association and affinity for other nuclear
446 structures. In contrast, Fibrillarin forms a separate spherical neocondensate when
447 deprived of its processing substrate rRNA, driven by strong self-association, and
448 Pitchoune, with strong self-association and a weak HP1a interaction motif, forms a
449 spherical neocondensate within the compacted PCH. Given the large number of multi-
450 component condensates within cells, it is crucial to assess whether new condensates
451 arise when perturbing interactions (e.g., by mutating a protein binding domain). Such
452 neomorphic responses, rather than the mutated protein itself, may cause defective
453 cellular phenotypes or behaviors. Understanding these outcomes will be important during
454 stress responses, aging, and cellular senescence when new condensates often form or
455 the composition of existing condensates changes [56].

Methods

Drosophila Stocks and Genetics

All crosses were maintained at 25° C. To visualize the dynamics of HP1a and nucleolar assembly, live embryos from _RFP-HP1a; GFP-Fib_, _RFP-Fib; GFP-HP1a_ and _RFP-HP1a; GFP-Mod_ stocks were imaged. Embryos lacking rDNA were obtained as described in Falahati et al. 2016 by crossing C(1)DX/Y; _RFP-HP1a; GFP-Fib_ or C(1)DX/Y; _RFP-HP1a; Pit-GFP_ or C(1)DX/Y; _RFP-Fib; Pit-GFP_ virgins to C(1;Y)6,y[1]w[1]f[1]/0 males. 1/4th of the resulting embryos from this cross lack rDNA, and -rDNA embryos were selected based on the presence of Fibrillarin neocondensates in live and fixed embryos and DAPI morphology in fixed embryos. To knockdown Pitchoune in eye discs, eyeless-GAL4 virgin females were crossed with Pitchoune RNAi VAL20 males, and eye discs were dissected from F1 third instar larvae.

Fly Genotype	Source
RFP-HP1a (2nd Chr)	Lipsick Lab (Wen et al., 2008)
GFP-HP1a (3rd Chr)	Lipsick Lab (Wen et al., 2008)
GFP-Fibrillarin	Weischaus Lab (Falahati and Wieschaus, 2017)
RFP-Fibrillarin	Weischaus Lab (Falahati et al., 2016)
GFP-Modulo	Weischaus Lab (Falahati and Wieschaus, 2017)
Pitchoune-GFP	Weischaus Lab (Falahati and Wieschaus, 2017)
FM6/C(1)DX, y[*] f[1]	BDSC # 784
C(1)RM/C(1;Y)6,y[1]w[1]f[1]/0	BDSC # 9460
Mat alpha GAL4	BDSC # 7063
Eyeless-GAL4	BDSC # 5534
Pitchoune RNAi VAL20	BDSC # 80368
Pitchoune RNAi VAL22	BDSC # 43984

Preparing _Drosophila_ embryos for live imaging

To collect _Drosophila_ embryos for live imaging, males and females of the desired genotype were added to a plastic cage covered with apple juice agar plates and left for at least 3 days at 25°C. On the day of imaging, a fresh plate was added to the cage, and embryos were collected for two hours. After removing the plate, embryos were coated with Halocarbon oil 27 (Sigma) for staging using a dissection scope with transillumination. Stage-selected embryos were placed on a 2 x 2 inch paper towel square and dechorionated in 50% bleach for 1 min. Bleach was wicked off with a Kimwipe after 1 min, the square was washed with a small amount of distilled water, and excess water was wicked off. Dechorionated embryos were secured onto a semipermeable membrane (Lumox film, Starstedt) on a membrane slide holder using Heptane Glue. These embryos were mounted in Halocarbon oil 27 (Sigma) between the membrane and a coverslip.

Immunostaining

Embryos were collected on apple juice-agar plates and aged till the appropriate stage, dechorionated in 50% bleach, fixed in 1:1 heptane:4% formaldehyde (Sigma) in 1XPBS for 25 mins, devitellinized in a 1:1 mixture of methanol:heptane, and stored at -20°C in methanol. Embryos were rehydrated by washing in 1xPBS+0.2% Triton (PBT). Dissected eye-discs were fixed in 4% formaldehyde in PBS for 20min, and the fixative was washed with PBT. Following washes with PBT, tissues were blocked for ~1hr with 2% BSA in PBT, then incubated with the primary antibody at 4°C overnight. After incubation with the appropriate secondary antibody at room temperature for 2 hrs, samples were stained in DAPI and mounted onto a slide using VectaShield (Vector Laboratories) mounting medium. All primary antibodies were used at 1:250 dilution and secondaries at 1:1000. Primary antibodies: Rabbit anti-Fibrillarin (Abcam ab5821), Mouse anti-H3K9me2 (Abcam ab1220), Rabbit anti-H3K9me3 (Abcam ab8898), Mouse anti-Modulo (Gift from Mellone Lab, from Chin-Chi Chen et al., 2012), Mouse anti-Lamin, Dm0 (DSHB ADL67.10). Secondary antibodies: Goat-anti-Mouse, Alexa Fluor 488 (Invitrogen A-11001), Goat-anti-Mouse, Alexa Fluor 568 (Invitrogen A-11004), Goat-anti-Rabbit, Alexa Fluor 488 (Invitrogen A-11034), Donkey-anti-Rabbit, Alexa Fluor 568 (Invitrogen A-10042).

DNA Fluorescent in situ hybridization (FISH) and combined Immuno-FISH

Probe Labelling

A probe for ITS-1 rDNA was prepared by amplifying an ~800 bp fragment by PCR from genomic DNA using the primers 5'-ACGGTTGTTTCGCAAAAGTT-3' and 5'-TGTTGCGAAATGTCTTAGTTTCA-3', cloned into a pGEM T-Easy vector (Promega) and used as a template for probe synthesis. ITS-1 rDNA probe was labeled with Alexa 488, Alexa 555, or Alexa 648 using the FISH Tag™ DNA Multicolor Kit (ThermoFisher) following the manufacturer's protocol. Locked nucleic acid (LNA) oligonucleotides (Integrated DNA technologies) conjugated with Cy5 or FAM were used as probes for 359bp, 1.686, and AAGAG satellite DNA repeats.

Hybridization

Embryos were collected on apple juice-agar plates and aged till the appropriate stage, dechorionated in 50% bleach, then fixed in 1:1 heptane: 4% formaldehyde in 1XPBS for 25 mins, devitellinized in a 1:1 mixture of methanol: heptane, and stored in -20°C. Embryos were washed in 2xSSC-T (2xSSC containing 0.1% Tween-20) with increasing formamide concentrations (20%, 40%, then 50%) for 15 min each. 100ng of DNA probes in 40 μl of hybridization solution (50% formamide, 3× SSCT, 10% dextran sulfate) was added, denatured together with the embryos at 95°C for 5 min and incubated overnight at 37°C. Following hybridization, embryos were washed twice in 2xSSCT for 30 mins at 37°C and thrice in PBT for 5 mins at room temperature. After completing washes, embryos

20

531 were stained in DAPI and mounted onto a slide using VectaShield (Vector Laboratories)
532 mounting medium.

Combined Immuno-FISH
534 Immunofluorescence was performed first on embryos for combined in situ detection of
535 proteins and DNA sequences. Embryos were post-fixed in 4% formaldehyde for 25 mins,
536 then processed for FISH.

Pan-Protein Staining using 488 NHS Ester
538 Formaldehyde-fixed embryos were devitellinized in a 1:1 mixture of methanol: heptane
539 and stored in methanol. Embryos were rehydrated by washing in 1xPBS+0.2% Triton
540 (PBT). After washing off methanol, embryos were stained in the diluted Atto 488 NHS
541 ester fluorophore (Sigma) (1:50) from a 10mg/ml stock in 0.1% PBST for 6 h at 4 °C
542 followed by washing in PBT three times for 30 mins each at room temperature. Embryos
543 were stained in DAPI for ten minutes and mounted onto a slide using VectaShield (Vector
544 Laboratories) mounting medium.

Propidium Iodide Staining
546 Formaldehyde-fixed and Heptane devitellinized embryos were rehydrated by washing in
547 1xPBS+0.2% Triton (PBT). Samples were equilibrated in 2X SSC. RNase-treated controls
548 alone were incubated in 100 µg/mL DNase-free RNase in 2X SSC for 20 minutes at 37°C.
549 After washing away the RNase with 2X SSC, embryos were incubated in 500nM of
550 Propidium Iodide (Invitrogen) in 2X SSC for 10 mins at room temperature. Samples were
551 rinsed in 2X SSC, stained with DAPI, and mounted on a slide with VectaShield (Vector
552 Laboratories) mounting medium.

Microscopy
554 Imaging was performed on a Zeiss LSM880 Airy Scan microscope (Airy Fast mode) with
555 a 63X NA 1.4 oil immersion objective at room temperature. Depending on the fluorophore,
556 405, 488, 514, or 633nm laser lines were used for excitation with appropriate filter sets.
557 Laser intensity values, detector gain, image size, zoom, z-stack intervals, and time
558 intervals (for time-lapse acquisitions) were adjusted to minimize bleaching and ensure
559 uniform detection across all AiryScan detection elements. Once standarized for an
560 experiment, settings were kept identical across all samples in the experimental groups.
561 Raw images were processed using Zeiss ZEN Black software with the AiryScan
562 processing module for reconstruction and subsequent image analysis.

Modeling
564 To better understand the association of PCH with the nucleolus, we developed a physical
565 model that simulates the interactions between different types of molecules found in these
566 biomolecular condensates. In our physical model, we simulate four components of the
567 nucleus: PCH (H) and ribosomal DNA (rD) as long polymers, and Fibrillarin (F) and an
568 amphiphilic protein (X) as independent, single monomers, which we hereafter refer to as

569 beads. Since the experiments focused on the PCH domain of *Drosophila*, our physical
570 model only simulates this specific region of the genome (30% of the genome), not the
571 entire genome. This allows us to study the dynamics of this particular region of the
572 genome more accurately and efficiently. PCH is modeled as a semiflexible bead-spring
573 polymer chain in which N beads are connected by N-1 harmonic springs. Each bead of
574 the chain represents a cluster of PCH containing approximately 5 kilo base pairs of DNA,
575 with a diameter of approximately 30 nm. The semi-flexibility of the chain is determined by
576 its persistence length, which is taken to be 60 nm (2 beads) in accordance with previous
577 studies that indicate chromatin has a persistence length between 50 to 100 nm
578 (Wachsmuth et al. 2016). We represent rDNA as a self-avoiding chain that occupies
579 approximately 20% of the middle domain of PCH. Fibrillarin and the amphiphilic protein
580 X are modeled using single, diffusive beads where each protein has distinct interactions
581 with the polymer and other proteins.

582 To simplify the model, we assume that the size of each protein bead is equal to the size
583 of the heterochromatin bead, with both having a diameter σ. The non-bonding interactions
584 between polymer-polymer, protein-protein, and polymer-protein are modeled using a
585 standard Lennard-Jones (LJ) potential. The LJ potential is truncated at the distance 2.5
586 σ, meaning that the interaction between the beads is only non-zero if they are within 2.5
587 σ distance. At very short distances between the beads, the LJ potential is strongly
588 repulsive (representing the excluded volume of two molecules). At intermediate spacings,
589 the LJ potential is attractive, with a strength adjusted to model the different states of
590 chromatin, such as its compaction or decondensation and the phase-separating tendency
591 of the proteins. In our model, the polymer and the proteins are confined within a spherical
592 boundary that represents the nucleus of the cell. This boundary mimics the effect of the
593 nuclear envelope, which constrains the movement of these beads and affects their
594 interactions with each other. In our study, we used the LAMMPS (Large-scale
595 Atomic/Molecular Massively Parallel Simulator) package to simulate the behavior of our
596 biomolecular system (Thompson et al. 2022). LAMMPS uses Brownian dynamics, which
597 accounts for the viscous forces acting on the beads, and a stochastic force (Langevin
598 thermostat) to ensure that the system of beads and solvent is maintained at a constant
599 temperature (NVT ensemble). This allows us to model the interactions between polymer-
600 polymer, polymer-protein, and protein-protein beads accurately and study the behavior of
601 the system over time.

602 **Rationale for the choice of parameters in the coarse-grained model**
603 To analyze the experimental observations of phase separation in the nucleus, we study a
604 minimal model with four crucial components: PCH (H), rDNA (rD), Fibrillarin (F), and an
605 amphiphilic protein (X) that binds both nucleolar and PCH components. The parameters
606 in the simulations include the number of molecules of each component α (N_α), the
607 strength of the attractions between two components (denoted by indices β and γ, $\epsilon_{\beta\gamma}$),

22

608   and the size of the confinement (R_c). The fraction of the nucleus that is hydrated (does
609   not contain PCH or the other proteins) is obtained from the relative difference between
610   the confinement volume and the volumes of PCH and the other proteins.

611   Bonding potential between monomers in the polymer made of PCH and rDNA: Adjacent
612   beads on the polymer chain are interconnected by harmonic springs using the potential
613   function:

614
$$V_s = \sum_{i=1}^{N-1} k_s (r_i - \sigma)^2$$

615   Here, r_i represents the distance between the i-th and $(i+1)$-th beads. The spring
616   constant and equilibrium distance between neighboring beads are denoted as k_s and σ
617   respectively. In our simulations, the spring constant k_s is set to $\frac{100\, k_B T}{\sigma^2}$ to ensure the
618   presence of rigid bonds between adjacent beads of the polymer chain.

619   Attraction strength ($\epsilon_{\beta\gamma}$): The Lennard-Jones potential is used to model the attraction
620   between any two non-bonded beads:

621
$$V_{\beta\gamma}(r) = 4\epsilon_{\beta\gamma} \left[\left(\frac{\sigma}{r}\right)^{12} - \left(\frac{\sigma}{r}\right)^6 \right] \text{ for } r \leq r_c \text{ and 0 for } r \leq r_c$$

622   Here, the symbol $\epsilon_{\beta\gamma}$ represents the attraction strength between beads of type β and γ,
623   where $\beta, \gamma \in \{H, rD, F, X\}$ represent PCH, rDNA, Fibrillarin, and amphiphilic protein,
624   respectively. For instance, ϵ_{FX} represents the attraction strength between Fibrillarin and
625   amphiphilic protein beads. When dealing with attractive interactions between chromatin-
626   chromatin and chromatin-protein beads, a distance cutoff of $r_c = 2.5\sigma$ is used for the
627   Lennard-Jones potential, beyond which the interaction is set to zero. To account for only
628   excluded volume interactions (with no attractions) using the same potential, a cutoff of
629   $r_c = 2^{1/6}\sigma$ and $\epsilon = 1 k_B T$ are employed. This choice is made because the potential energy
630   is at its minimum at that point, and the resulting force on a bead is zero. As there are four
631   components in our model, there are a total of 10 combinations (n(n+1)/2), where n is
632   number of components, of attraction strength parameters between the different
633   components.

634   Confinement size: The size of the confinement is determined by defining the volume
635   fraction of chromatin ϕ:

636
$$\phi = N_G \times \frac{\text{volume of 1 bead}}{\text{volume of confinement}} = N_G \times \frac{\left(\frac{4}{3}\pi\sigma^3\right)}{\left(\frac{4}{3}\pi R_c^3\right)}$$

23

637 Here, N_G represents the total number of beads in the *Drosophila* genome, where each
638 bead corresponds to 5 kilobase pairs (kbps) of DNA. The diameter of a spherical bead,
639 denoted as σ, is taken to be 30 nm (see [59] for further explanation). The total length of the
640 diploid *Drosophila* genome is 360 Mbps, and N_G can be calculated by dividing the
641 *Drosophila* genome length by the amount of DNA represented by one bead (5 kbps). The
642 volume fraction of chromatin (ϕ) is commonly reported as ~ 0.1 in existing literature (Qi
643 & Zhang, 2021; Tripathi & Menon, 2019). Using the equation above, the calculated radius
644 of the confinement (R_c) is found to be 45σ.

645 <u>Number of molecules in PCH and rDNA:</u> We model the PCH domain as a polymer chain
646 composed of $N = 10{,}000$ beads, which represents approximately 30% of the beads in the
647 entire genome. Among these 10,000 beads, 20% are designated as rDNA, resulting in a
648 total of $4{,}000$ rDNA beads. We do not explicitly model the rest of the genome since the
649 experiments show that the nucleolar components are localized near PCH.

650 <u>Concentration of Fibrillarin and amphiphilic protein:</u> The concentration of Fibrillarin and
651 amphiphilic protein is calculated as follows:

652
$$\text{concentration } (c_\alpha) = \frac{N_\alpha}{\text{volume of confinement}}$$

653 Here, the symbol α represents the type of protein, where $c_\alpha = c_F$ for the fibrillarin
654 concentration and $c_\alpha = c_X$ for the amphiphilic protein concentration. After defining the
655 parameters and obtaining the value for the confinement radius parameter from the
656 assumed volume fraction of PCH, we proceed with an initial simulation, focusing on a
657 single component, namely the Fibrillarin protein, within the confinement. During this
658 simulation, we vary the concentration (c_F) and the attraction strength (ϵ_{FF}) of Fibrillarin.
659 Our experimental results demonstrate that Fibrillarin undergoes phase separation
660 independently of the other components (rDNA or PCH) during cycle 14 (refer to Figure
661 2A). These initial-stage simulation results yield a phase diagram, which indicates that a
662 minimum attraction strength of $1.3 - 2.0 k_{\mathrm{B}}\mathrm{T}$ is required to condense fibrillarin particles
663 within the concentration range of $c_F = 0.0013 - 0.013$. The reported concentration of
664 nucleolar particles is $c = 0.015$ (Qi & Zhang, 2021). Consequently, we maintain a fixed
665 concentration of Fibrillarin at $c_F = 0.013$ when simulating all the other protein components
666 (**Extended Data Fig. 4a**). Since the concentration of amphiphilic protein is not determined
667 from the experiments, we conducted multiple simulations, systematically varying the
668 amphiphilic protein concentration (c_X) within the range of $0.0013 - 0.13$. The results of
669 these simulations are discussed in **Fig. 6a-b**.

670 <u>Parameter range of ϵ_{HH}:</u> To understand the behavior of each component separately
671 (before including interactions between different components) in the next stage, we
672 conducted simulations specifically focusing only on the PCH chain. The PCH chain
673 represents a condensed chromatin region within the nucleus which implies self-attractive

674   interactions of the beads representing the polymer. During these simulations, we varied
675   the attraction strength between PCH beads (ϵ_{HH}) from 0 to $0.5k_\mathrm{B}$T. Our results revealed
676   that within the range of $\epsilon_{HH} = 0.35 - 0.5\ k_\mathrm{B}$T (**Extended Data Fig. 4b**), the PCH chain
677   underwent collapse, resulting in a condensed conformation that is phase-separated from
678   the aqueous component of the system (not simulated explicitly).

679   Parameter value of ϵ_{rD-F}: We next simulate the self-organization due to the interactions
680   between the three components (where each component so far was considered alone):
681   PCH, rDNA, and Fibrillarin. We set $\epsilon_{HH} = 0.35\ k_\mathrm{B}$T and $\epsilon_{FF} = 2\ k_\mathrm{B}$T, incorporating only
682   excluded-volume interactions (hard-core, repulsive interactions) between H-F, i.e., there
683   is no direct attraction between PCH and Fibrillarin as implied by the experiments. By
684   varying the attraction strength between rDNA and Fibrillarin (ϵ_{rD-F}), we made the
685   following observations based on our simulation results: a weaker attraction (and $\epsilon_{rD-F} =$
686    $0.75\ k_\mathrm{B}$T) resulted in rDNA wrapping around the condensed Fibrillarin phase, while a
687   stronger attraction (and $\epsilon_{rD-F} = 2\ k_\mathrm{B}$T) led to the condensation of rDNA within the
688   Fibrillarin complex. This latter observation aligns with our experimental findings.
689   Therefore, we select $\epsilon_{rD-F} = 2\ k_\mathrm{B}$T as the parameter value in the subsequent simulations
690   (**Extended Data Fig. 4c**).

691   Parameter ranges of ϵ_{FF} and ϵ_{XX}: Finally, we introduce the fourth component, an
692   amphiphilic protein 'X', which we suggest may interact attractively with both PCH and
693   Fibrillarin. Initially, we investigated the relative attraction strengths between Fibrillarin and
694   protein X when considering the same concentration for both. We explore all possible
695   combinations of ϵ_{FF} both greater than and less than ϵ_{XX}. For $\epsilon_{XX} \geq \epsilon_{FF}$, we observe PCH
696   surrounding the amphiphilic protein-rich phase, but just a partial wetting between the
697   amphiphilic protein-rich phase and the Fibrillarin-rich phase (**Extended Data Fig. 4d**).
698   Only when $\epsilon_{XX < } \epsilon_{FF}$ do we observe PCH surrounding the amphiphilic protein-rich phase,
699   which in turn surrounds the Fibrillarin condensate, consistent with the experimental
700   results in wild type embryos.

701   Parameter range of ϵ_{FX}: We proceeded to vary the attraction strength between Fibrillarin
702   and amphiphilic protein X within the range of $\epsilon_{FX} = 1.5k_\mathrm{B}$T. When the attraction strength
703   is relatively low ($\epsilon_{FX} \leq 0.75k_\mathrm{B}$T), the fibrillarin-rich phase and the amphiphilic protein-rich
704   phase do not associate with each other. At moderate attraction strengths ($\epsilon_{FX} \geq 1k_\mathrm{B}$T and
705   ($\epsilon_{FX} \leq 1.25k_\mathrm{B}$T), the Fibrillarin-rich and amphiphilic protein-rich phases partially wet each
706   other. Finally, at higher attraction strengths ($\epsilon_{FX} = 1.5k_\mathrm{B}$T), the amphiphilic protein
707   completely wets Fibrillarin (**Extended Data Fig. 4e-f**).

708   Parameter range of c_X: Additionally, we explored variations in the concentration of
709   amphiphilic protein X (c_X). Notably, for higher concentrations of protein X ($c_X = 0.005 -$
710   0.013), we observed that heterochromatin tends to completely engulf the amphiphilic
711   protein-rich phase, which in turn engulfs Fibrillarin (**Fig. 6a**).

Cell culture

Drosophila S2 cells were cultured in Schneider's *Drosophila* Medium (Gibco) with 10% FBS and 1% antibiotic-antimycotic (Gibco) at 25°C. For transfections, cells were seeded at 5 x 10^5 cells/mL in 6-well plates 24 hours prior. 1 µg of plasmid DNA was diluted in 100 µL of serum-free medium and mixed with 2 µL of TransIT-2020 Transfection Reagent (Mirus Bio). After a 15-min incubation, the DNA-reagent complexes were added to the cells and incubated at 25°C for 48-72 hours before visualizing.

Plasmids/Recombinant DNA

Codon-optimized gene blocks for Pitchoune, Fibrillarin, Modulo, Polr1E, and HP1a were synthesized by Twist Biosciences and cloned into pCOPIA vectors fused with fluorescent protein tags. Site-directed mutagenesis was performed to introduce PxVxL and DQVD mutations into the full-length Pitchoune using the Q5® Site-Directed Mutagenesis Kit (New England Biolabs) using these primers:

Pit^{PxVxL}_F: CCGGTAGAAGATCTCAAAGAAGGAGCTGCTAAGCG
Pit^{PxVxL}_R: CGGTACCAGGAAGCCGAAAC
Pit^{DQVD}_F: CCAAGTCGACAGGATCCTGG
Pit^{DQVD}_R: TCGATGATGAGGCACTGCAA

Pitchoune RNAi

Genomic DNA from S2 cells was used as the template for PCR amplification with the primers listed below to generate the amplicon for Pitchoune RNAi targeting its 3' untranslated region (3'UTR). Mock RNAi targeting the y gene was used as a negative control.

T7-Pit-RNAi-F: TAATACGACTCACTATAGGgctgctttacttgagtgtgtgt
T7-Pit-RNAi-R: TAATACGACTCACTATAGGccaaggtggcccgcaattat
T7-Mock-RNAi-F: TAATACGACTCACTATAGGgaaaaactaagccaacgtcatc
T7-Mock-RNAi-R: TAATACGACTCACTATAGGgccgtggatataggcaaaaa

Hi-Scribe T7 Synthesis kit (New England Biolabs) was used to synthesize double-stranded RNA (dsRNA) using manufacturer's protocol. Following synthesis, RNA purification was carried out utilizing the MinElute RNeasy Kit (Qiagen). The purified RNA was then diluted to 1 µg/µl. For the RNAi experiment, 3-5 µg of dsRNA with DOTAP liposomal transfection reagent (Roche) was used per 0.5 x 10^6 cells. Cells were analyzed 5 or 6 days after the initiation of RNAi.

Total RNA Preparation, cDNA Synthesis, and Quantitative PCR

Total RNA from S2R+ cells was extracted by homogenizing in TRIzol Reagent (Invitrogen). 0.5 volume of chloroform was added, the mixture was shaken for 15 seconds, incubated for 3 minutes, and centrifuged at 12,000 x g for 15 minutes at 4°C. The aqueous phase was transferred to a new tube, mixed with 500 μL of isopropanol, incubated for 10 minutes, and centrifuged at 12,000 x g for 10 minutes at 4°C. The RNA pellet was washed with 75% ethanol, centrifuged at 7,500 x g for 5 minutes at 4°C, air-dried for 5-10 minutes, and resuspended in RNase-free water. Total RNA was treated with DNA-free DNA removal kit (Invitrogen) per manufacturer's protocol to remove any contaminating genomic DNA. RNA was converted to cDNA with GoScript Reverse Transcriptase Kit (Promega) using random primers, and Real-Time PCR was performed using PerfeCTa SYBR® Green FastMix (Quantabio) on the Biorad CFX96 Real-Time PCR Detection system. Analysis was performed using the $2^{-\Delta\Delta Ct}$ method, with relative mRNA levels of Pitchoune normalized to β-actin.

Quantitative Image Analysis

3D measurements were performed using Arivis Vision4D (Zeiss) while ImageJ was used for all 2D measurements. The details of each analysis pipeline used in this study are listed below:

<u>Measuring the fraction of the nucleolar edge occupied by HP1a or H3K9me2</u>

Fig. 1c: Nuclei were manually chosen for analyses ~15-30 mins into the specified interphase and defined as "Early Cycle ", while those observed from ~50-70 mins were defined as "Late Cycle ". Preprocessing steps include background subtraction and denoising using Gaussian blur. HP1a and Fibrillarin were segmented in 3D using the "Intensity Threshold Segmenter" with the Auto segmentation method. To calculate HP1a occupancy at the nucleolar edge, the nucleolus was dilated by 1 pixel and subtracted from the dilated object to create a 1-pixel shell around the nucleolus. The nucleolus shell was intersected with HP1a segments to calculate the volume fraction of the nucleolar shell that overlaps with HP1a.

Fig. 6c: Same as above, except the nucleolus was dilated by 2 pixels to create a 2-pixel shell around the nucleolus. The shell was intersected with H3K9me2 segments in nuclei from eye-discs to calculate the fraction of the nucleolar shell that overlaps with H3K9me2.

Fig. 6e: Same as above, except the nucleolus was dilated by 4 pixels to generate a 4-pixel shell around the nucleolus. The thickness of the nucleolar shell scaled with nucleolar size in the different cell types.

<u>Measuring Distances</u>

Fig. 2b: HP1a and Fibrillarin were segmented using the "Intensity Threshold Segmenter" with the Auto segmentation method. The distance between HP1a and its nearest Fibrillarin segment was measured in 3D using the "Distances" feature in Arivis.

27

775   Fig. 2f: AAGAG and 1.686 were segmented using the "Intensity Threshold
776   Segmenter" with the Auto segmentation method. The distance between AAGAG and its
777   nearest 1.686 segment was measured in 3D using the "Distances" feature in Arivis.

778   Extended Data Fig. 2e: Preprocessing steps include background subtraction and
779   denoising using Gaussian blur. 1.686 or 359bp foci and Fibrillarin were manually
780   segmented using the "Intensity Threshold Segmenter" with the Simple segmentation
781   method. The distance between a Fibrillarin segment and its nearest 1.686 or 359bp locus
782   was measured in 3D using the "Distances" feature in Arivis.

783   Measuring Aspect Ratio of HP1a

784   Fig. 2d: Individual nuclei were manually selected 15 mins after the start of Cycle
785   15. Preprocessing steps include background subtraction and denoising using Gaussian
786   blur. HP1a was segmented using Auto thresholding using Otsu. The aspect ratio of the
787   segment was determined using the Analyze Particles feature in Fiji.

788   Line Scans:

789   Fig. 6g: Nucleoli were segmented in Fiji using Otsu's method. The Feret's diameter
790   was calculated for each nucleolus, and intensity values were measured along the Feret's
791   diameter. Intensities for each profile were normalized to its average value. The Feret's
792   diameter was normalized by setting its range from 0 to 1.

793   Pitchoune neo-condensate formation measurements

794   Fig. 5d-f: To measure the dynamics of the formation of Pitchoune in -rDNA
795   embryos, maximum intensity projections of Amnioserosa were first preprocessed in Fiji
796   using Subtract background and a Gaussian Blur filter. Auto thresholding for each time
797   point was performed using the Yen method. Using Analyze Particles, the area, circularity,
798   and mean intensity of each segment of Pitchoune was extracted. The mean intensity over
799   time was normalized to its value at T=0.

Statistical Analysis

801   Data were plotted, and statistical analyses were performed using GraphPad Prism8. P-
802   values were calculated using unpaired two-tailed t-tests.

Data availability statement

804   All data supporting the results of this study are included in the manuscript. Reagents used
805   in this study are available upon request.

Code availability statement

807   For the simulation component of this study, all simulations, analyses, and visualizations
808   were conducted using publicly available software packages and custom-developed
809   codes. Langevin Dynamics simulations were performed using LAMMPS (version 23 June
810   2022), and visualizations were generated using Ovito (version 3.7.11). The complete set
811   of codes required to reproduce the simulations is available in the following

28

812　repository: https://github.com/gauravbajpaimaths/Coarse-
813　grained_model_of_nucleolar_heterochromatin_condensates

AUTHOR CONTRIBUTIONS

820　SR: conceptualization, experimentation, data acquisition, formal analysis, validation,
821　investigation, methodology, and writing
822　OA: conceptualization, investigation, formal analysis, and writing
823　GB: simulations, data acquisition, formal analysis, methodology, and writing
824　KL: experimentation and data acquisition
825　SC: experimentation, data acquisition, reagent preparation, and formal analysis
826　SS: writing, funding acquisition, and supervision
827　GHK: conceptualization, writing, funding acquisition, and supervision

**COMPETING INTERESTS**

829　No competing interests to declare.

BIBLIOGRAPHY

1. Strom, A. R. & Brangwynne, C. P. The liquid nucleome – phase transitions in the nucleus at a glance. *J Cell Sci* **132**, jcs235093 (2019).

2. Misteli, T. The Self-Organizing Genome: Principles of Genome Architecture and Function. *Cell* vol. 183 Preprint at https://doi.org/10.1016/j.cell.2020.09.014 (2020).

3. Shin, Y. & Brangwynne, C. P. Liquid phase condensation in cell physiology and disease. *Science (1979)* **357**, eaaf4382 (2017).

4. Lyon, A. S., Peeples, W. B. & Rosen, M. K. A framework for understanding functions of biomolecular condensates on molecular to cellular scales. *Nat Rev Mol Cell Biol* **22**, 215 (2021).

5. Ditlev, J. A., Case, L. B. & Rosen, M. K. Who's In and Who's Out—Compositional Control of Biomolecular Condensates. *J Mol Biol* **430**, 4666–4684 (2018).

6. Fare, C. M., Villani, A., Drake, L. E. & Shorter, J. Higher-order organization of biomolecular condensates. *Open Biol* **11**, 210137 (2021).

7. Pederson, T. The nucleolus. *Cold Spring Harb Perspect Biol* **3**, 1–16 (2011).

8. Feric, M. *et al.* Coexisting Liquid Phases Underlie Nucleolar Subcompartments. *Cell* **165**, 1686–1697 (2016).

9. Lafontaine, D. L. J., Riback, J. A., Bascetin, R. & Brangwynne, C. P. The nucleolus as a multiphase liquid condensate. *Nat Rev Mol Cell Biol* **22**, 165–182 (2020).

10. Riback, J. A. *et al.* Composition-dependent thermodynamics of intracellular phase separation. *Nature 2020 581:7807* **581**, 209–214 (2020).

11. King, M. R. *et al.* Macromolecular condensation organizes nucleolar sub-phases to set up a pH gradient. *Cell* **187**, 1889-1906.e24 (2024).

12. Padeken, J. & Heun, P. Nucleolus and nuclear periphery: Velcro for heterochromatin. *Curr Opin Cell Biol* **28**, 54–60 (2014).

13. Bizhanova, A. & Kaufman, P. D. Close to the edge: Heterochromatin at the nucleolar and nuclear peripheries. *Biochim Biophys Acta Gene Regul Mech* **1864**, 194666 (2021).

14. Janssen, A., Colmenares, S. U. & Karpen, G. H. Heterochromatin: Guardian of the Genome. *Annu Rev Cell Dev Biol* **34**, 265–288 (2018).

15. Politz, J. C. R., Scalzo, D. & Groudine, M. Something Silent This Way Forms: The Functional Organization of the Repressive Nuclear Compartment. *Annu Rev Cell Dev Biol* **29**, 241–270 (2013).

16. Eissenberg, J. C. & Elgin, S. C. The HP1 protein family: getting a grip on chromatin. *Curr Opin Genet Dev* **10**, 204–210 (2000).

17. Keenen, M. M. *et al.* HP1 proteins compact DNA into mechanically and positionally stable phase separated domains. 1–30 (2020).

18. Larson, A. G. *et al.* Liquid droplet formation by HP1α suggests a role for phase separation in heterochromatin. *Nature* **547**, 236–240 (2017).

19. Strom, A. R. *et al.* Phase separation drives heterochromatin domain formation. *Nature* **547**, 241–245 (2017).

20. Wang, L. *et al.* Histone Modifications Regulate Chromatin Compartmentalization by Contributing to a Phase Separation Mechanism. *Mol Cell* 1–14 (2019) doi:10.1016/j.molcel.2019.08.019.

21. Tortora, M. M. C., Brennan, L. D., Karpen, G. & Jost, D. HP1-driven phase separation recapitulates the thermodynamics and kinetics of heterochromatin condensate formation. *Proc Natl Acad Sci U S A* **120**, (2023).

22. McClintock, B. The relation of a particular chromosomal element to the development of the nucleoli in Zea mays. *Zeitschrift für Zellforschung und Mikroskopische Anatomie* **21**, 294–326 (1934).

23. Quinodoz, S. A. *et al.* Higher-Order Inter-chromosomal Hubs Shape 3D Genome Organization in the Nucleus. *Cell* **174**, 744-757.e24 (2018).

24. Bersaglieri, C. *et al.* Genome-wide maps of nucleolus interactions reveal distinct layers of repressive chromatin domains. *Nature Communications 2022 13:1* **13**, 1–18 (2022).

25. Carvalho, C. *et al.* Chromosomal G-dark bands determine the spatial organization of centromeric heterochromatin in the nucleus. *Mol Biol Cell* **12**, 3563–3572 (2001).

26. Dillinger, S., Straub, T. & Németh, A. Nucleolus association of chromosomal domains is largely maintained in cellular senescence despite massive nuclear reorganisation. *PLoS One* **12**, e0178821 (2017).

27. Wang, Y. & DiMario, P. Loss of Drosophila nucleostemin 2 (NS2) blocks nucleolar release of the 60S subunit leading to ribosome stress. *Chromosoma* **126**, 375–388 (2017).

28. Farrell, J. A. & O'Farrell, P. H. From Egg to Gastrula: How the Cell Cycle Is Remodeled During the Drosophila Mid-Blastula Transition. *Annu Rev Genet* **48**, 269–294 (2014).

29. Falahati, H., Pelham-Webb, B., Blythe, S. & Wieschaus, E. Nucleation by rRNA dictates the precision of nucleolus assembly. *Current Biology* **26**, 277–285 (2016).

30. Warsinger-Pepe, N., Li, D. & Yamashita, Y. M. Regulation of Nucleolar Dominance in Drosophila melanogaster. *Genetics* **214**, 991–1004 (2020).

31. Greil, F. & Ahmad, K. Nucleolar Dominance of the Y Chromosome in Drosophila melanogaster. *Genetics* **191**, 1119–1128 (2012).

32. Pontvianne, F. *et al.* Subnuclear partitioning of rRNA genes between the nucleolus and nucleoplasm reflects alternative epiallelic states. *Genes Dev* **27**, 1545–1550 (2013).

33. Berry, J. *et al.* RNA transcription modulates phase transition-driven nuclear body assembly. *Proc Natl Acad Sci U S A* **112**, E5237–E5245 (2015).

31

902 34. Lacy, M. E. & Hutson, M. S. Amnioserosa development and function in Drosophila
903   embryogenesis: Critical mechanical roles for an extraembryonic tissue. *Developmental*
904   *Dynamics* **245**, 558–568 (2016).

905 35. M'Saad, O. & Bewersdorf, J. Light microscopy of proteins in their ultrastructural context.
906   *Nature Communications 2020 11:1* **11**, 1–15 (2020).

907 36. Falahati, H. & Wieschaus, E. Independent active and thermodynamic processes govern
908   the nucleolus assembly in vivo. *Proceedings of the National Academy of Sciences* **114**,
909   1335–1340 (2017).

910 37. Torza, S. & Mason, S. G. Coalescence of Two Immiscible Liquid Drops. *Science (1979)*
911   **163**, 813–814 (1969).

912 38. Kelley, F. M., Favetta, B., Regy, R. M., Mittal, J. & Schuster, B. S. Amphiphilic proteins
913   coassemble into multiphasic condensates and act as biomolecular surfactants. *Proc Natl*
914   *Acad Sci U S A* **118**, e2109967118 (2021).

915 39. Zaffran, S. *et al.* A Drosophila RNA helicase gene, pitchoune, is required for cell growth
916   and proliferation and is a potential target of d-Myc. *Development* **125**, 3571–3584 (1998).

917 40. Thiru, A. *et al.* Structural basis of HP1/PXVXL motif peptide interactions and HP1
918   localisation to heterochromatin. *EMBO J* **23**, 489 (2004).

919 41. Smothers, J. F. & Henikoff, S. The HP1 chromo shadow domain binds a consensus
920   peptide pentamer. *Current Biology* **10**, 27–30 (2000).

921 42. Overwijn, D. & Hondele, M. DEAD-box ATPases as regulators of biomolecular
922   condensates and membrane-less organelles. *Trends Biochem Sci* **48**, 244–258 (2023).

923 43. Zhang, H. *et al.* DEAD-Box Helicase 18 Counteracts PRC2 to Safeguard Ribosomal DNA
924   in Pluripotency Regulation. *Cell Rep* **30**, 81-97.e7 (2020).

925 44. Pause, A. & Sonenberg, N. Mutational analysis of a DEAD box RNA helicase: the
926   mammalian translation initiation factor eIF-4A. *EMBO J* **11**, 2643–2654 (1992).

927 45. Hug, C. B. & Vaquerizas, J. M. The Birth of the 3D Genome during Early Embryonic
928   Development. *Trends Genet* **34**, 903–914 (2018).

929 46. Sawh, A. N. *et al.* Lamina-Dependent Stretching and Unconventional Chromosome
930   Compartments in Early C. elegans Embryos. *Mol Cell* **78**, 96-111.e6 (2020).

931 47. Aguirre-Lavin, T. *et al.* 3D-FISH analysis of embryonic nuclei in mouse highlights several
932   abrupt changes of nuclear organization during preimplantation development. *BMC Dev*
933   *Biol* **12**, 1–20 (2012).

934 48. Bizhanova, A., Yan, A., Yu, J., Zhu, L. J. & Kaufman, P. D. Distinct features of nucleolus-
935   associated domains in mouse embryonic stem cells. *Chromosoma* **129**, 121–139 (2020).

936 49. Ogienko, A. A., Korepina, M. O., Pindyurin, A. V. & Omelina, E. S. New Functional Motifs
937   for the Targeted Localization of Proteins to the Nucleolus in Drosophila and Human Cells.
938   *Int J Mol Sci* **25**, (2024).

50. Dembowski, J. A., Kuo, B. & Woolford, J. L. Has1 regulates consecutive maturation and processing steps for assembly of 60S ribosomal subunits. *Nucleic Acids Res* **41**, 7889 (2013).

51. Boeynaems, S. *et al.* Poly(A)-binding protein is an ataxin-2 chaperone that regulates biomolecular condensates. *Mol Cell* **83**, 2020-2034.e6 (2023).

52. Padeken, J. *et al.* The Nucleoplasmin Homolog NLP Mediates Centromere Clustering and Anchoring to the Nucleolus. *Mol Cell* **50**, 236–249 (2013).

53. Holmberg Olausson, K., Nistér, M. & Lindström, M. S. Loss of nucleolar histone chaperone NPM1 triggers rearrangement of heterochromatin and synergizes with a deficiency in DNA methyltransferase DNMT3A to drive ribosomal DNA transcription. *Journal of Biological Chemistry* **289**, 34601–34619 (2014).

54. Sanchez-Burgos, I., Joseph, J. A., Collepardo-Guevara, R. & Espinosa, J. R. Size conservation emerges spontaneously in biomolecular condensates formed by scaffolds and surfactant clients. *Scientific Reports 2021 11:1* **11**, 1–10 (2021).

55. Schmit, J. D., Feric, M. & Dundr, M. How Hierarchical Interactions Make Membraneless Organelles Tick Like Clockwork. *Trends Biochem Sci* **46**, 525–534 (2021).

56. Alberti, S. & Hyman, A. A. Biomolecular condensates at the nexus of cellular stress, protein aggregation disease and ageing. *Nature Reviews Molecular Cell Biology 2021 22:3* **22**, 196–213 (2021).

57. Wachsmuth, M., Knoch, T. A. & Rippe, K. Dynamic properties of independent chromatin domains measured by correlation spectroscopy in living cells. *Epigenetics Chromatin* **9**, 1–20 (2016).

58. Thompson, A. P. *et al.* LAMMPS - a flexible simulation tool for particle-based materials modeling at the atomic, meso, and continuum scales. *Comput Phys Commun* **271**, 108171 (2022).

59. Bajpai, G. & Safran, S. Mesoscale, long-time mixing of chromosomes and its connection to polymer dynamics. *PLoS Comput Biol* **19**, e1011142 (2023).
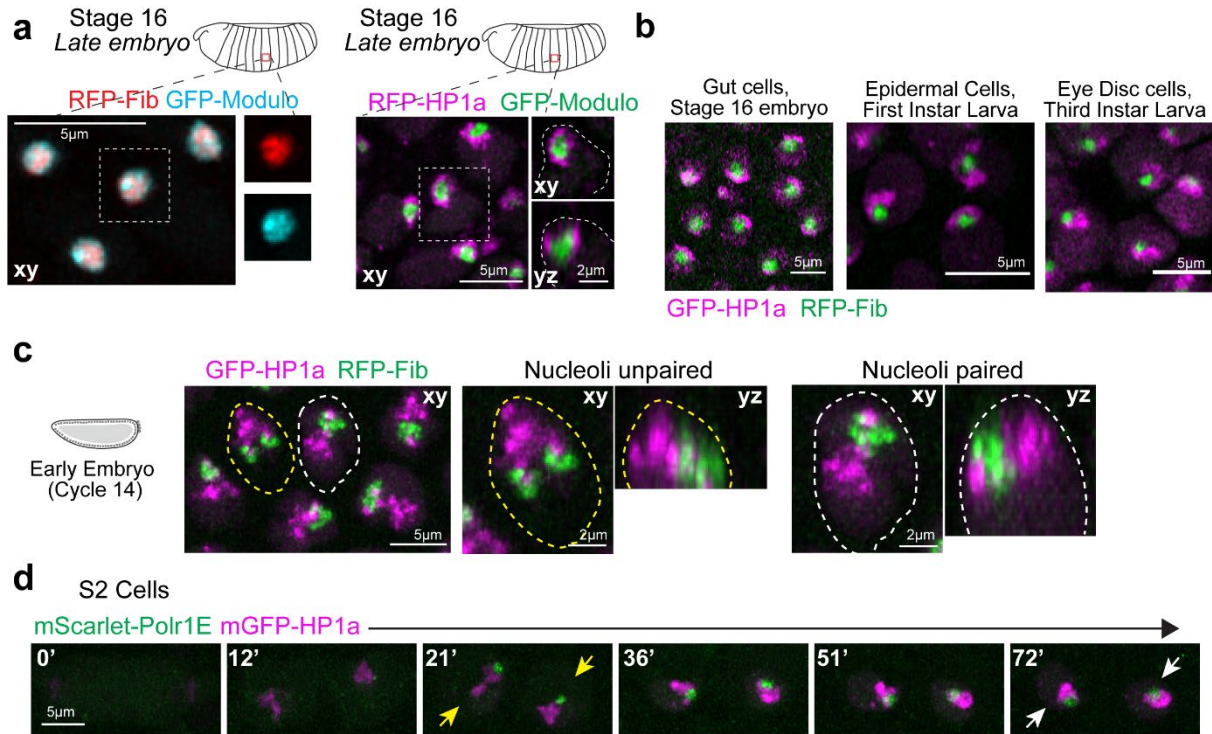
Extended Data Fig. 1: PCH organization relative to the nucleolus in Drosophila embryos, larval tissues, and cultures cell lines. (**a**) (Left) Distribution of GFP-Modulo (cyan) and RFP-Fibrillarin (red) in nucleoli of a live late-stage (Stage 16) embryo. (Right) Maximum intensity projections showing PCH localization labeled with RFP-HP1a (magenta) and nucleoli marked by GFP-Modulo (green) in live epidermal nuclei from a late-stage *Drosophila* embryo (Stage 16, ~14-16hr). The nucleus outlined by the white dashed box is magnified and presented in xy and xz views, with white dashed lines indicating the nuclear boundary. (**b**) Stills of live nuclei expressing GFP-HP1a (magenta) and RFP-Fib (green) in gut cells from a Stage 16 embryo, first instar larval epidermal cells, and third instar larval eye disc. (**c**) Nuclei from Cycle 14 embryos expressing GFP-HP1a (magenta) and RFP-Fib (green), showing two unpaired nucleoli (yellow dashed line) and one paired nucleolus (white dashed line). Both nuclei have been enlarged to show the "extended" conformation of HP1a relative to the nucleolus in the xy and yz views. (**d**) Time-lapse stills of two daughter S2 cells exiting mitosis, transfected with mScarlet-Polr1E, a Pol-I subunit (green) and mGFP-HP1a (magenta). Numbers on the top left corner indicate time in minutes from the end of mitosis. Yellow arrows indicate HP1a in an extended conformation from the nucleolus, while white arrows indicate HP1a in the surrounded conformation.

34
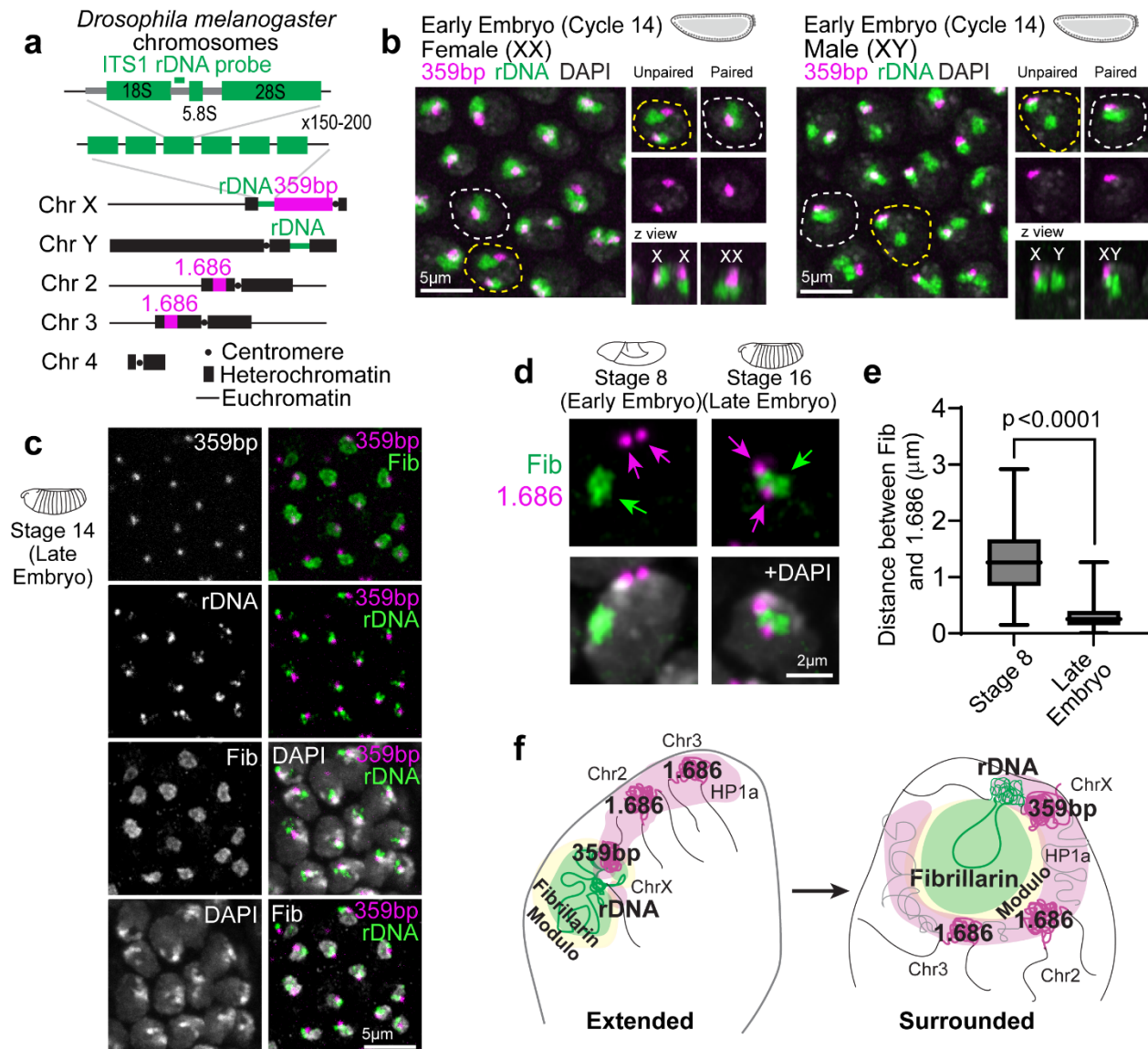
Extended Data Fig. 2: Dynamics of PCH reorganization relative to the nucleolus during *Drosophila* embryonic development. (**a**) Schematic representation of pericentromeric satellite repeats (359bp and 1.686) and rDNA repeats in *Drosophila* melanogaster chromosomes. The schematic of ribosomal DNA (rDNA) arrays indicates the position of the ITS-1 rDNA probe used for FISH. (**b**) Localization of 359bp satellite DNA (magenta) and rDNA (green) in female and male early (Cycle 14) embryos. The dashed white line indicates a nucleus with paired nucleoli, while the dashed yellow line marks a nucleus with unpaired nucleoli. The nuclear boundary is determined by DAPI staining. (**c**) Combined immuno-FISH stained for 359bp, ITS-1 rDNA, Fibrillarin, and DAPI in late embryos. (**d**) Combined immuno-FISH of 1.686 (magenta arrows), Fibrillarin (green arrow) and DAPI (grey) in a nucleus from epidermal cells of early (Stage 8, ~Cycle 15) and late (Stage 16) *Drosophila* embryos. (**e**) Distance between the centers of geometry of 1.686 and Fibrillarin in Stage 8 (~Cycle 15) and Stage 16 (Late) in *Drosophila* nuclei. n>60 loci (from 3 embryos) at each developmental stage. Bar graphs extend from 25th to 75th percentile, error bars: min to max. (**f**) Schematic summarizing the dynamic reorganization of nucleoli and PCH during *Drosophila* development, highlighting key proteins and DNA elements involved.
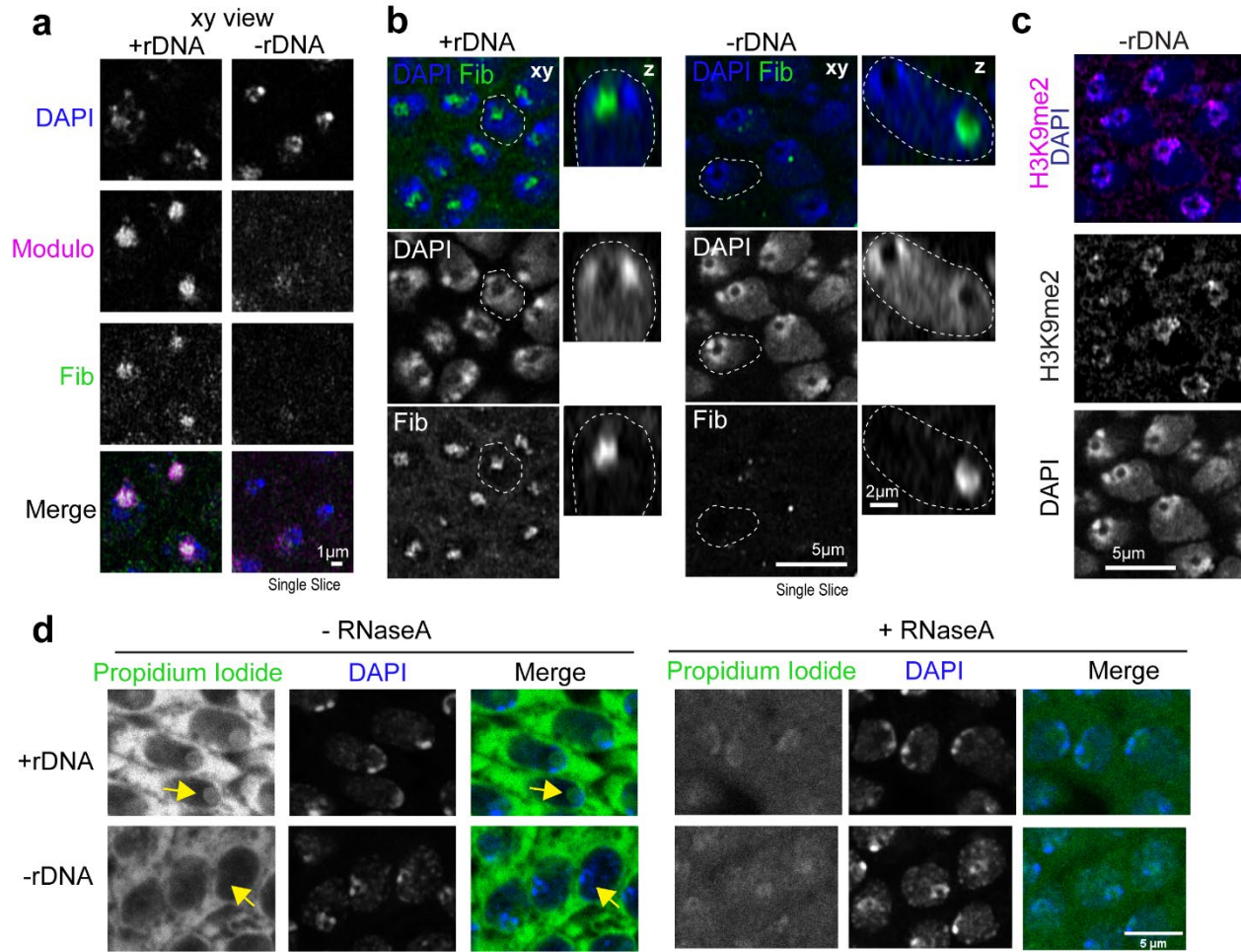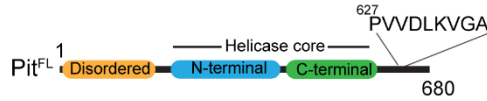
Extended Data Fig. 3: The PCH void in -rDNA embryos does not stain for DAPI, Fibrillarin, Modulo, H3K9me2 or Propidium Iodide (RNA). (**a**) Representative images of fixed nuclei from wildtype late embryos and mutant embryos lacking rDNA stained for Modulo (magenta), Fibrillarin (green) and DAPI (blue). (**b**) Left: Representative images of fixed nuclei from Stage 14-16 (late) wildtype embryos and mutant embryos lacking rDNA showing Fibrillarin (green) and DAPI (blue). Right: Nuclei marked with white dashed outlines on the left are shown in the z plane. (**c**) H3K9me2 immunofluorescence (magenta) and DAPI (blue) staining in -rDNA nuclei in Stage 14-16 (late) *Drosophila* embryos. (**d**) Representative images of fixed nuclei from Stage 14-16 (late) wildtype and mutant embryos lacking rDNA stained with Propidium Iodide (green) and DAPI (blue) without (left) and with (right) RNaseA. The yellow arrow points to the RNA staining in the nucleolus in +rDNA and lack of propodium iodide staining in the PCH void of -rDNA nuclei.

36
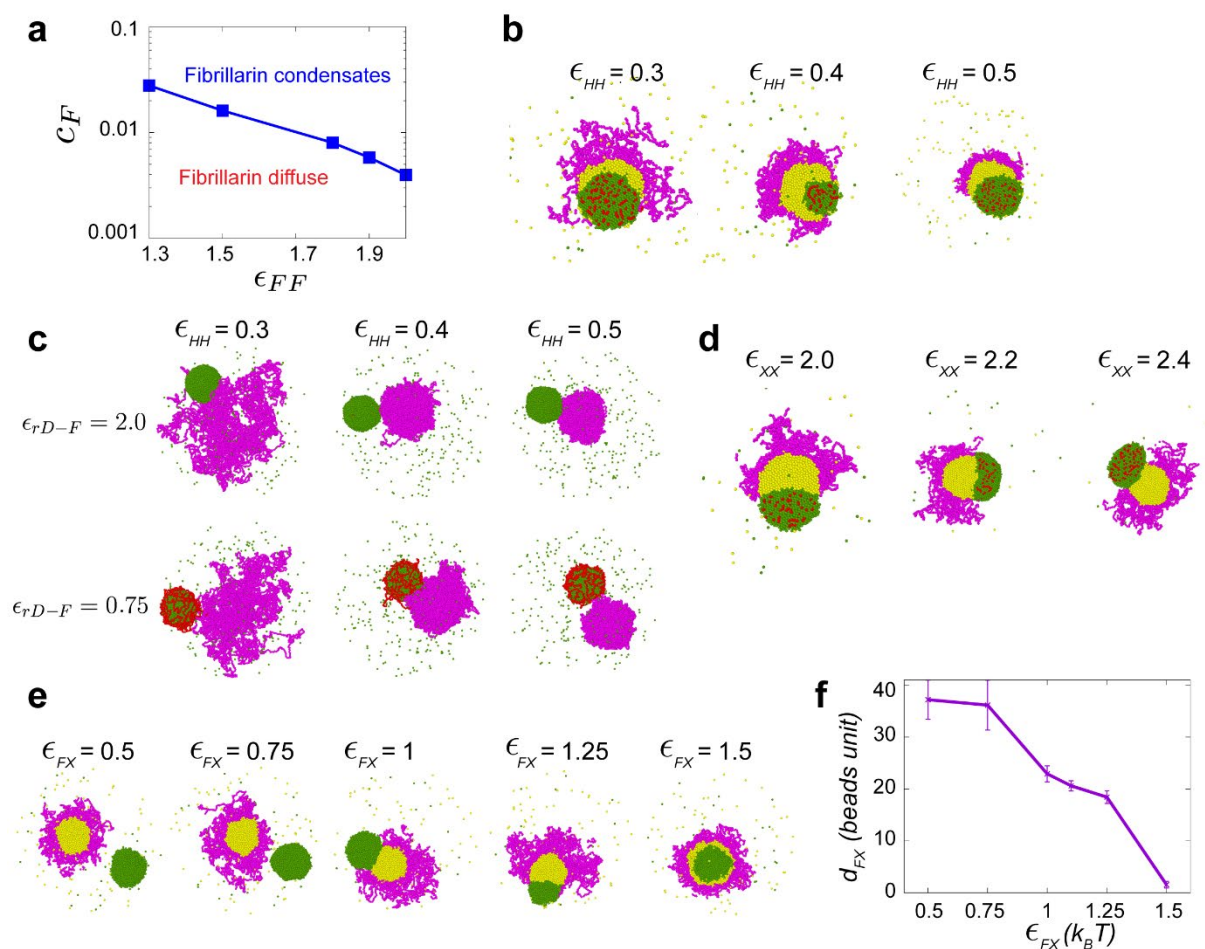
Extended Data Fig. 4: Coarse-grained model for the assembly of the nucleolus and PCH. (**a**) The phase diagram illustrates the minimum attraction strength required to condense Fibrillarin at different concentrations. (**b**) Simulation endpoint snapshots depict the outcomes of varying the attraction strengths between beads of the PCH (H) polymer chain (ϵ_{HH}). (**c**) Simulation snapshots depict varying attraction strengths between rDNA-Fibrillarin (top to bottom) and beads of the PCH polymer chain (left to right). (**d**) Simulation endpoint snapshots depict the outcomes of varying X-X attraction strengths (ϵ_{XX}). (**e**) Simulation endpoint snapshots depict the outcomes of varying attraction strengths between Fibrillarin and protein X (ϵ_{FX}) in the -rDNA condition. (**f**) The average distance (d_{FX}) between Fibrillarin and protein X condensates from their center of mass is measured for different attraction strengths. Error Bars represent s.d.

a


```
                                                        627
                                                       PVVDLKVGA
                                          Helicase core
                              Pit^FL  1  Disordered  N-terminal  C-terminal
                                                                      680

Alignment within Drosophila:

D. melanogaster Pit   IFNVNTLDLQAVAKSFGFLVPPVVDLKVGAAKRERPEKRVGGGGFGFYKKMNE-GSASKQ
D. simulans           IFNVNTLDLQAVAKSFGFLVPPVVDLKVGAAKRERPEKRVGGGGFGFYKKMNE-GSASKQ
D. sechellia          IFNVNTLDLQAVAKSFGFLVPPVVDLKVGAAKRERPEKRVGGGGFGFYKKMNE-GSASKQ
D. yakuba             IFNVNTLDLQAVAKSFGFLVPPVVDLKVGAAKRERPEKRVGGGGFGFYKKMNE-GSASKQ
D. erecta             IFNVNTLDLQAVAKSFGFLVPPVVDLKVGAAKRERPEKRVGGGGFGFYKKMNE-GSASKQ
D. virilis            IFNVNTLDLQAVSKSFGFLVPPVVDLKVGAAKRERPEKRVGGGGFGYYKQMNDSGA--KQ
D. mojavensis         IFNVNTLDLQAVAKSFGFLVPPVVDLKVGAAKRERPEKRVGGGGFGYYKQMNERGGGHKQ
D. persimilis         IFNVNTLDLQAVSKSFGFLVPPVVDLKVGAAKRQRPEKRVGGGGFGYYRQMND-TSASKQ
D. pseudoobscura      IFNVNTLDLQAVSKSFGFLVPPVVDLKVGAAKRQRPEKRVGGGGFGYYRQMND-TSASKQ
D. ananassae          IFNVNTLDLQAVAKSFGFLVPPVVDLKVGAAKRERPEKRVGGGGFGYYKKMNE-GSDSKQ
D. grimshawi          IFNVNTLDLQAVSKSFGFLVPPVVDLKVGAAKRERPEKRVGGGGFGYYKQMNDNSS--KQ
D. willistoni         IFNVNTLDLQAVAKSFGFLVPPVVDLKVGAAKRQRPEKRMGGGGFGYYKQMND---TNKQ
                      ************ ****************** ***** ****** *  **       **

Alignment across species:

D. melanogaster Pit   QIFNVNTLDLQAVAKSFGFLVPPVVDLK--VGAA-KRERPEKRVGGGGFGFYKKMNE
D. rerio ddx18        QIYNVETLDLPKVAMSFGFKVPPFVDLN--VHSS-KGVKLHKRGGGGGFGYQKSKN-
H. sapiens DDX18      QIFNVNNLNLPQVALSFGFKVPPFVDLN--VNSN-EG-KQKKRGGGGGFGYQKTKK-
M. musculus Ddx18     QIFNVNNLNLPQVALSFGFKVPPFVDLN--VSSH-DG-KLKKRGGGGGFGYQKTKK-
C. elegans B0511.6    DIFDVTNMDLTAVSKSFGFSVPPFVDLP--ISNK-PKVEIRSKLSGAGYRKKKQSFT
S. pombe has1         SIFDINKLDLAKVAKSFGFAHPPNVNIT--IGAS-GR--TDKKERRAGYNKKNHVDV
S. cerevisiae HAS1    TVYQIDKLDLAKVAKSYGFPVPPKVNIT--IGAS-GK--TPNTKRR-----KTHK--
A. thaliana AT3G18600 EIFDVSKLSIENFSASLGLPMTPRIRFT..VGAEMRKADIEDKKVDKERRREKRMKQ
                                         *  *      *
```
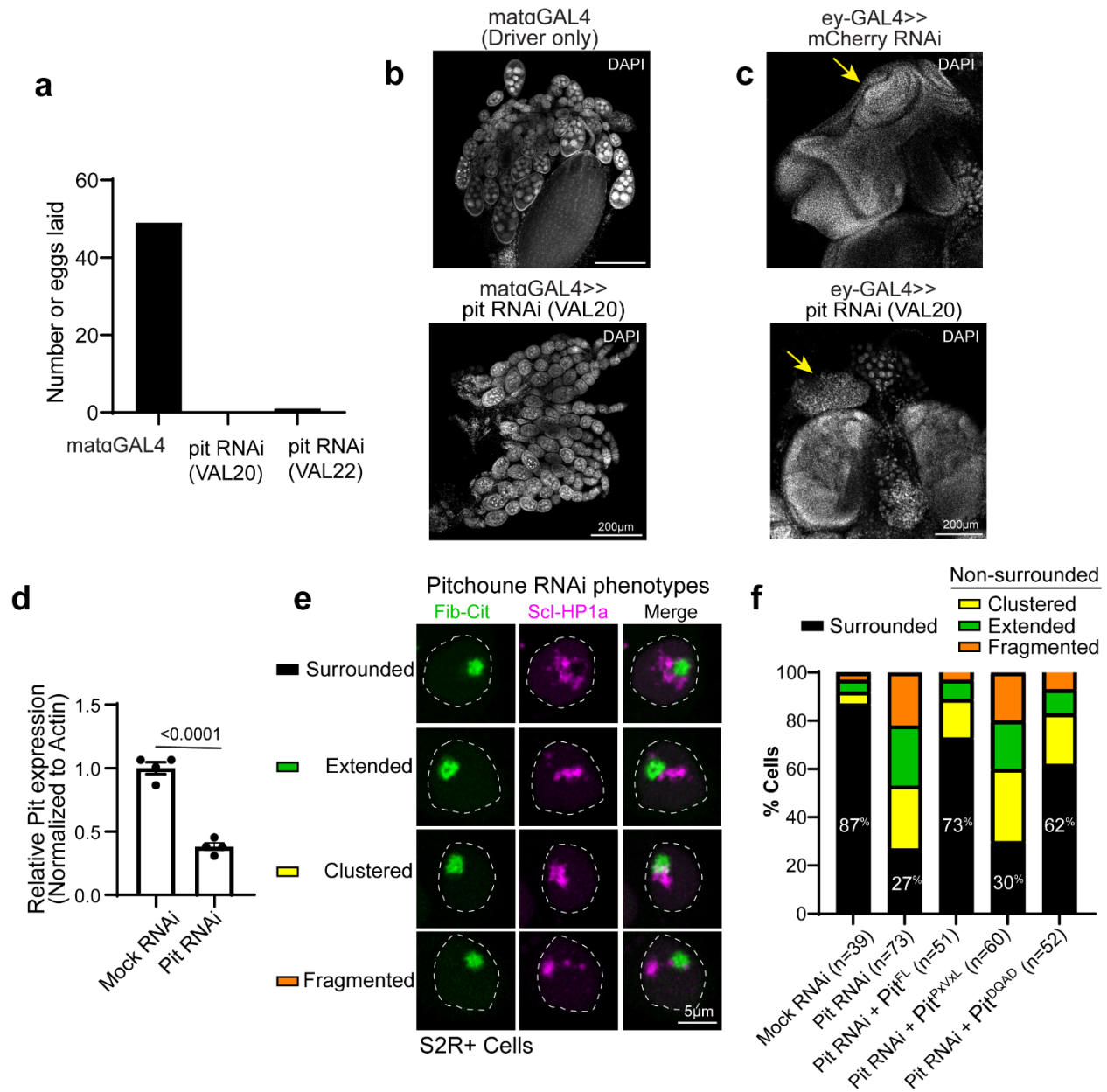
Extended Data Fig. 5: Pitchoune has a conserved PxVxL HP1a-interacting motif. (**a**) Evolutionary analysis to determine the conserved PxVxL motif in Pitchoune within *Drosophila* species (top) and across non-*Drosophila* eukaryotic model organisms (bottom).

Extended Data Fig. 6: Developmental defects and HP1a disorganization phenotypes due to Pitchoune knockdown in Drosophila tissues and cultured cells. (**a**) Number of eggs laid on an apple juice plate after a 3hr collection in mataGAL4 (driver only) and mataGAL4 driving UAS-Pitchoune RNAi (VAL20 and VAL22 lines). (**b**) Representative images of dissected ovaries in control (mataGAL4, driver only) and after Pitchoune knockdown stained with DAPI. (**c**) Representative images of dissected eye antennal discs (yellow arrow) in control (ey-GAL4>mCherry RNAi) and after Pitchoune knockdown (ey-GAL4>pit RNAi, VAL20) stained with DAPI. (**d**) Quantitation of Pitchoune transcripts using qPCR to confirm the knock-down of Pitchoune, normalized to actin. Bar graphs depict mean ± s.e.m. n=4 biological replicates. (**e**) Representative nuclei transfected with Fib-Citrine and Scarlet-I-HP1a, showing four categories of HP1a distribution phenotypes observed after Pitchoune knockdown. (**f**) Quantification of the % nuclei with Surrounded, Extended, Clustered, and Fragmented HP1a phenotype after Pitchoune RNAi and its rescue with Pit^{FL}, Pit^{PxVxL}, and Pit^{DQVD}.

39

LEGENDS FOR SUPPLEMENTARY MOVIES

966 **Supplementary Movie 1:** 3D rendering of RFP-Fib (green) and GFP-HP1a (magenta) in
967 epidermal cells of a Stage 16 Drosophila embryo.

968 **Supplementary Movie 2:** Live imaging of RFP-Fib (green) and GFP-HP1a (magenta) in nuclear
969 cycle 13 of Drosophila embryogenesis.

970 **Supplementary Movie 3:** Live imaging of RFP-Fib (green) and GFP-HP1a (magenta) in nuclear
971 cycle 14 of Drosophila embryogenesis.

972 **Supplementary Movie 4:** Live imaging of RFP-Fib (green) and GFP-HP1a (magenta) in nuclear
973 cycle 15 of Drosophila embryogenesis.

974 **Supplementary Movie 5:** Live imaging of RFP-Fib (green) and GFP-HP1a (magenta) in nuclear
975 cycle 16 of Drosophila embryogenesis.

976 **Supplementary Movie 6:** Live imaging of RFP-Fib (green) and GFP-HP1a (magenta) in nuclear
977 cycle 17 of Drosophila embryogenesis.

978 **Supplementary Movie 7:** Live imaging of GFP-Fib (green) and RFP-HP1a (magenta) in nuclear
979 amnioserosa nuclei in embryos lacking rDNA.

980 **Supplementary Movie 8:** Simulations of coarse-grained modeling of rDNA (red), Fibrillarin
981 (green), PCH (magenta), and an amphiphilic protein (yellow) with the parameters listed in the 4X4
982 matrix in Fig. 4c.

983 **Supplementary Movie 9:** Live imaging of Pitchoune-GFP (green) and RFP-HP1a (magenta) in
984 nuclear amnioserosa nuclei in embryos lacking rDNA.